**APPLICATIONS OF TIGHTLY FOCUSED ULTRAFAST LASER
IN THE FABRICATION OF MICRO TOTAL ANALYSIS SYSTEMS AND
BIOLOGICAL RESEARCH**

by

Kevin Ke

A dissertation submitted in partial fulfillment
of the requirements for the degree of
Doctor of Philosophy
(Biomedical Engineering)
in The University of Michigan
2008

Doctoral Committee:

    Associate Professor Alan J. Hunt, Chair
    Professor Edgar Meyhöfer
    Associate Professor Shuichi Takayama
    Assistant Professor Mohamed E H El-Sayed
    Assistant Professor Michael Mayer

© Kevin Ke

DEDICATION

To Ajit, Damon, Boyle, and Alan

To family and friends

To space and future

ACKNOWLEDGEMENTS

TABLE OF CONTENTS

LIST OF TABLES

LIST OF FIGURES

Figure   **Page**

ABSTRACT

**APPLICATIONS OF TIGHTLY FOCUSED ULTRAFAST LASER
IN THE FABRICATION OF MICRO TOTAL ANALYSIS SYSTEMS AND
BIOLOGICAL RESEARCH**

by

Kevin Ke

Chair: Alan J. Hunt

Tight focusing of femtosecond pulses accentuates the non-linear effect of optical breakdown to achieve damage regions smaller than the light resolution limit. When pulse energy is near the breakdown threshold, optical breakdown using tightly focused ultrafast laser is extraordinary precise and induces minimal collateral damage. These characteristics enable the surgical manipulation of sub-cellular structures and its importance becomes apparent when dealing with intrinsically mechanical cellular processes such as mitosis.

We examine the role of polar ejection forces (PEFs) in guiding directional instability of vertebrate mitotic chromosomes. Taking advantage of extremely precise character of femtosecond pulsed laser microsurgery, we abruptly alter PEFs by severing chromosome arms. Reduction of PEFs increases the amplitude of directional instability without altering other characteristics, or the speed of chromosome movement. We find

that PEFs limit the range of chromosome oscillation by increasing the probability that motors at a leading kinetochore abruptly fail or disengage, leading to a direction reversal. From the relation between the change in oscillation amplitude and the length of the chromosome arm shortened, we are able to map the distribution of PEFs across spindle, which is surprisingly different from distributions previously assumed. These results allow us to differentiate between models of directional instability, and reveal relations between forces within the spindle and chromosome movements fundamental to the intrinsically mechanical mitotic process.

In the course of developing this surgical technique, we fabricated devices such as nanochannels and resistive-pulsed sensors in glass in order to study the capabilities of laser-induced optical breakdown. We found microbubbles created with this technique highly damped and contribute little collateral damage compared to shockwave-forming cavitation bubbles produced by longer pulsed lasers. In their own right, these studies contribute to the field of medical diagnosis and biodefense by establishing methods capable of speeding up chemical separation and detection of viruses. Transitioning from glass to cells, we studied the effect of microsurgical removal of proteinaceous ASC aggregates, which play an important role in inflammatory diseases.

CHAPTER 1

INTRODUCTION

Laser-induced optical breakdown by femtosecond pulses is extraordinary precise when the pulse energy is near the breakdown threshold. Tightly focusing of the femtosecond pulses accentuates the non-linear effect of optical breakdown to limit the damage region to a volume smaller than the light resolution limit. The combination of these two capabilities with video microscopy and nanometer-precise positioning system into a single tool enables selective targeting and ablation of any desired location. This ability, applicable on both the surface and the inside of a transparent dielectric medium, can solve many known problems. These problems, including rapid prototyping of nanofluidics in glass substrates and functional study of multi-protein complexes, are nearly impossible to solve with conventional techniques such as HF etching of glass and gene-knockout for example. This is particularly true when one of the proteins in the multi-protein complex is required for maintaining cell vitality or for the formation of the complex. Yet, these problems can be efficiently solved with techniques described in this manuscript.

1.1. Physics of Optical Breakdown

Before we can effectively use ultrafast lasers for problem solving, we must understand some of its basic principles. The most important being the breakdown mechanism. In essence, optical breakdown by ultrafast lasers is a nonlinear process that involves a seeding stage (multiphoton ionization and/or Zennel tunneling) and a secondary stage (avalanche ionization). This eventually leads to bound electrons becoming free electrons and a formation of plasma. Depending on the type of the laser (continuous wave, nanosecond, picosecond, or femtosecond pulsed-laser), the damage region can be as small as the volume occupied by the plasma or much bigger. The details of the optical breakdown process can be found in Joglekar *et al.*, 2004.

1.2. Implication of Breakdown Mechanism

This mechanism of the material damage exhibits certain beneficial properties when induced by lasers with pulse duration shorter than a picosecond. One of these benefits is the relatively low pulse energy required to reach optical breakdown threshold. As pulse duration reduces, the energy required to reach the breakdown threshold of the material reduces accordingly and so does the size of the ablation (Loesel *et al.*, 1996). One possible explanation is the absorbing effect of the plasma. Plasma is a heavy light absorber. It can transfer large amount of energy from the laser to the material lattice and cause ill-defined thermal damage, for example, through melting. The short duration of the femtosecond laser reduces the amount of energy available after plasma formation. This in effect limits the damage region to a well-defined volume of the plasma.

Consequentially, holes produced by femtosecond laser ablation have less than 1% variation in size, while nanosecond has 10-20% (Du *et al*., 1994, Joglekar *et al*., 2003).

To break apart a material, enough valence electrons must be ionized into plasma. So the homogeneity of valence electron is important in determine repeatability of the ablation size. Therefore, as long as the seeding of free electron is consistent, laser induced damage should be uniform and repeatable. Femtosecond laser pulses, having high enough intensity, are capable of reliably generating the seed electrons required for sustainable avalanche ionization. What this means is that femtosecond lasers are capable of producing precise and reproducible damage to mixed and amorphous materials such as glass and cell wall (Ke *et al*., 2005a), and, as we will see later on, chromosome and protein structures (Chapter 4 and 5).

1.3. Practice of Laser Machining

By lowering the laser pulse energy close to the breakdown threshold that is at "critical intensity", optical breakdown becomes extraordinarily precise and enables reproducible laser machining of sub-diffraction limit features on surfaces with a sub-picosecond laser (Du *et al*., 1995; Joglekar *et al*., 2004; Pronko *et al*., 1995; Liu *et al*., 1997; Schaffer *et al*., 2001; Venkatakrishnan *et al*., 2002). The precision down to the nanoscale has recently been demonstrated by producing surface features on the order of 10 nm (Joglekar *et al*., 2003; Joglekar *et al*., 2004). I have further demonstrated that nanometer scale features can also be reliably fabricated in gold (Ke *et al*., 2005a). Also, by subtractively removing layers of connected 30 nm holes, I have produced surface trenches that are 30 nm in width and 500 to 1000 nm in depth (Ke *et al*., 2005a). Thus,

optics at critical intensity (OCI) nanomachining can produce features at a scale that competes with e-beam lithography, a surface process, but requires less sample preparation, does not need a vacuum environment, and is less material-specific.

Interestingly, these trenches are suitable for building structures using traditional multilayered methods. For example, nanometer fluidic channels can be built by sintering (forming a coherent mass by heating without melting) a glass wafer with nanometer trenches to one without. The trenches could then be used for increasing surface area for chemical analytical applications or for making high throughput filters. But as we will see below, direct machining of sub-micrometer channel inside of glass is possible because laser-induced optical breakdown does not have to be a surface only process, and can in fact create 3D structures inside of glass.

One of the major barriers to practical laser machining of material is the ultimate destination of ablated materials. Ablated materials may be re-deposited at or near the site of breakdown, creating unintended structures or debris at the machining site (Joglekar *et al.*, 2004; Li *et al.*, 2001; Marcinkevicius *et al.*, 2001). This becomes an especially significant problem during the machining of deep channels or other subsurface features since the entrenched debris causes optical scattering and interference of the laser beam and prevents further machining. It also prevents the extrusion of new debris. I investigated using expanding bubbles that are produced during machining as a mechanism to extrude fluid entrained debris. I found that by submersing the glass target in water and tightly focusing the laser, debris-free, sub-surface structures can be machined as easily as surface structures. The machining of high-aspect ratio and sub-micrometer diameter channels and the debris extrusion mechanism are discussed in

Chapter 3. Direct machining of glass using tightly focused femtosecond laser has certain advantages over HF etching of glass. For example, access to HF determines the etching profile and prevents the fabrication of long or deep structures in glass. In addition, laser machining of glass is a one-step process and does not require masks or clean room. Laser machining is ideal for rapid prototyping because it is highly amenable to making on-the-fly changes and testing new designs.

The advantage of femtosecond laser machining becomes even more evident when an application that requires removal of large amount of material also demands high level of accuracy, and a complex profile. An example application is a laser-fabricated device that detects the aggregation of nano-particles called "nanopore". This device, machined in glass, consists of a shank tens of micrometers in diameter, hundreds of micrometers in length, but ends with a conical tip that opens to the other side of the glass. The tip opening is only a few hundred nanometers. Continuous wave and pulsed lasers with duration longer than a few picoseconds have difficulty leaving a smooth bottom after cutting away the shank much less creating a conical profile with a small tip opening. We accomplish this by cutting the shank with laser energy many times the glass breakdown threshold to speed up material removal. Then, we reduce the pulse energy so it is near the breakdown threshold that is at OCI to ensure a precise tip opening.

The rapid prototyping capability of tightly focused ultrafast laser at OCI enables testing of many tip profiles. I was able to find a profile that offers both machinability and low capacitance. The capacitance of the nanopore becomes very important when it is used as a resistive-pulse sensor. This type of sensor, commonly known as coulter counter, detects changes in electrical conductance as conductive fluid containing particles

flow through a small aperture, in this case, the sub-micrometer tip of a glass nanopore. For example, a non-conductive particle, as it passes through the aperture, would decrease the effective cross-section of the conductive channel and increase the resistance. Low capacitance, both from the conical profile and from the choice of material, offers lower noise and enables detection of smaller particles. The performance of sensors based on glass nanopore is evaluated in Uram *et al.*, 2007. These nanopores are used to monitor the formation of antibody-antigen complexes (Uram *et al.*, 2006a) and the interaction of antibody and viruses (Uram *et al.*, 2006b).

1.4. Minimizing Collateral Damage

Critical to the successful laser machining of sub-micrometer channels are the micro-bubbles produced during machining. These bubbles are unlike typical cavitation bubbles (Vogel *et al.*, 1996) that have diameters a thousand times bigger and collapse time a thousand times shorter. Unlike typical cavitation bubbles, these bubbles do not have supersonic speeds at the bubble wall during the final moments of collapse, which produce shockwaves that cause unwanted collateral damage. Instead, these micro-bubbles are highly damped and surprisingly long-lived. As a result, instead of diminishing the accuracy of machining due to unintended damages associated with their violent collapse, they enable machining of long and deep structures underneath the surface by gently extruding the debris. More information on this, both theoretical and practical, can be found in Chapter 3.

Bubble and shockwave formation are but two among many mechanisms of collateral damage. Others factors are discussed in Chapter 2. But as we shall see,

femtosecond lasers, especially when the laser energy is slightly above the breakdown threshold, have the majority of the laser energy going into initiating plasma formation instead of producing collateral damage. Figure 1.1 illustrates the merit of tightly focused ultrafast laser at OCI over other modes of laser ablation.
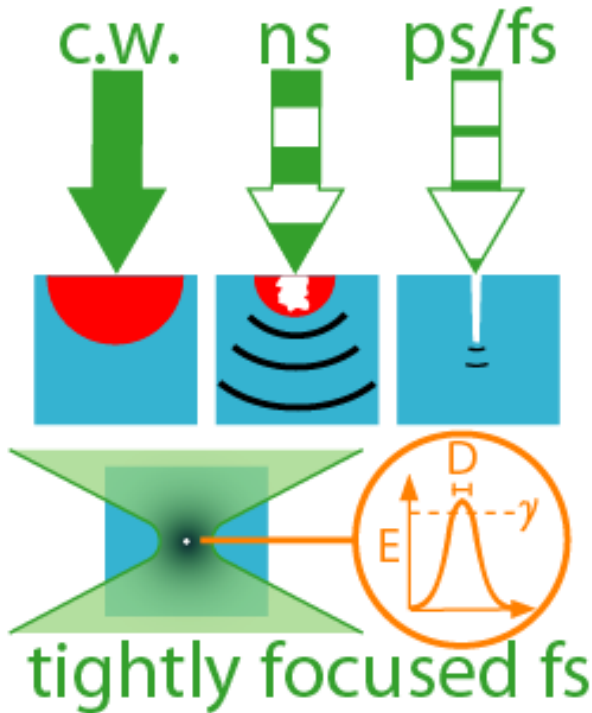
Figure 1.1. The advantage of tightly focused ultrafast laser at OCI over other forms of laser ablation. Continuous wave (c.w.) laser has a large thermally induced damage region. Nanosecond (ns) pulsed laser has ill-defined optical breakdown, and smaller but still significant thermal damage. Strong shockwave produced by the cavitation bubble causes additional collateral damage. Pico- and femto-second (ps/fs) laser produces well-defined optical breakdown and small amount of shockwaves. Tightly focused ultrafast laser at OCI combines threshold-dependency of nonlinear optical breakdown with Gaussian profile of the laser to produce well-defined ablation smaller than the focus spot. Its pulse duration, energy, and small ablation size minimize thermal-induced damage, shockwave production, and other sources of collateral damage.

1.5. Laser in Biology

Having identified the setup and the parameter in which a laser does minimal collateral damage to a system, I applied this technique to study two of the most important

processes in biology – mitosis (Chapter 4) and apoptosis (Chapter 5). Specifically, for the study of mitosis, I was looking for ways to manipulate chromosome. In the past, this has been done with microneedles, whether metallic or stretched from a glass pipette. However, they are highly invasive, have poor spatial resolution, and are difficult to operate. For example, the length of the microneedle inserted into the cell displaces large amount of cellular material. In addition, it also punctures the plasma membrane that isolates the cell from its environment. Tightly focused ultrafast laser at OCI, on the other hand, only does damage where the laser intensity is above the breakdown threshold. This means that although the laser must pass through the cell membrane and a large volume of the cell, it does no damage except where it is intended, which could be as small as a thousandth of a micrometer cube in volume. Thus, I was able to successfully sever chromosome arms and study the mechanism of mitosis.

In my investigation of apoptosis, I needed a way to remove a multi-protein complex known as "speck". The formation of speck involves a protein called "ASC". The exact composition of the speck is unknown; therefore, it was impossible to use gene-knockout, RNAi, and antibody-inhibition. Presumably, by using gene-knockout or RNAi, I could prevent ASC from expressing itself and disable apoptosis. However, I was intrigued by the formation of the speck. The speck grows from nothing to micrometers in size within minutes. In the process, it depletes nearly all of the ASCs in the cell. What we want to know is whether the formation of the speck initiates the apoptotic cascade or results from the accumulation of by-products in the apoptotic pathway. Timing, in this case, is important. To solve the problem, the speck must be removed only after it is formed. Tightly focused ultrafast laser at OCI is the solution to this problem. Because

the limited collateral damage of this technique, it is capable of removing a large portion of cell without killing the cell. This has been successfully demonstrated and will be discussed in Chapter 5.

1.6. Example Applications

I examined the physical mechanism of laser-induced optical breakdown. From the mechanism, I point out the benefit of ultrafast laser at OCI over its competitors. The three most important benefits of this system are precision, limited collateral damage, and rapid prototyping. We will now look at three applications in detail.

The first application, discussed in Chapter 3, is in the area of Micro Total Analysis Systems (μTAS). Microfluidic and nanofluidic technologies have long sought a fast, reliable method to overcome the creative limitations of planar fabrication methods, the resolution limits of lithography, and the materials limitations for fast prototyping. In the present work, we demonstrate direct 3D machining of sub-micrometer diameter, subsurface fluidic channels in glass, via optical breakdown near critical intensity, using a femtosecond pulsed laser. No post exposure etching or bonding is required; the channel network (or almost any arbitrary-shaped cavity below the surface) is produced directly from "art-to-part". The key to this approach is to use very low energy, highly focused, pulses in the presence of liquid. Microbubbles that result from laser energy deposition gently expand and extrude machining debris from the channels. These bubbles are in a highly damped, low Reynolds number regime, implying that surface spalling due to bubble collapse is unimportant. We demonstrate rapid prototyping of three-dimensional

"jumpers", mixers, and other key components of complex 3D microscale analysis systems in glass substrates.

The second application, discussed in Chapter 4, is in the area of mitosis. We examine the role of polar ejection forces (PEFs) in guiding directional instability of vertebrate mitotic chromosomes. Taking advantage of extremely precise character of femtosecond pulsed laser microsurgery, we abruptly alter PEFs by severing chromosome arms. We find the reduction of PEFs increases the amplitude of directional instability without altering other characteristics of directional instability or the speed of chromosome movement. This implies that the kinetochore motor assemblies exhibit load independence, and constrains the possible mechanism by which kinetochores generate forces and maintain attachments to spindle microtubules. The PEFs limit the range of chromosome oscillation by increasing the probability that all force-generating motors at a leading kinetochore abruptly fail or disengage, leading to a direction reversal. From the relation between the change in oscillation amplitude and the length of the chromosome arm shortened, we are able to map the distribution of PEFs across spindle, which is surprisingly different from distributions previously used in models of directional instability. These results allow us to differentiate between models of directional instability, and reveal relations between forces within the spindle and chromosome movements fundamental to the intrinsically mechanical mitotic process.

The third application, discussed in Chapter 5, is in the area of apoptosis. ASC is a 22-kDa adapter protein composed of a PYD and a CARD domain that is capable of interacting with proteins upstream of IL-1β and NF-κB (see Chapter 5 for more detail). Through its interacting partners, ASC affects a wide spectrum of pathways critical to

apoptotic and inflammatory events. The activation of the apoptotic pathway in ASC expressing cells often coincides with the formation of an ASC aggregate widely known as a "speck". Although cells with specks progress to apoptosis, it is not clear if the speck is a byproduct or is required for the mediation of the apoptotic process. I studied the functional role of the speck through a technique called structural knockout. An ultrafast laser was used to physically remove the speck from transfected HeLa cells in a surgical procedure called "speckectomy". In contrast to gene knockout, RNAi, and antibody inhibition, this procedure allows spatial and temporal control over the removal of particular sub-cellular structures in cells. Ablation using tightly focused ultrafast laser pulses virtually eliminates the collateral damage that is typically associated with laser microsurgery. Our real time tracking of the life cycle of cells expressing ASC and forming a speck revealed that over 48 hours, 60 percent of such cells die, 30 percent undergo mitosis, and 10 percent undergo unsuccessful mitosis. In contrast, cells in which the speck is removed by speckectomy, 75 percent undergo mitosis; 25 percent undergo unsuccessful mitosis. In the speckectomized cells that undergo mitosis, mitotic duration and morphology is normal. The survival of cells that undergo speckectomy is nearly identical to control cells that express ASC but do not form specks: 75 percent mitosis and 25 percent cell death. This result supports the notion that the physical aggregate known as the speck participates actively in the apoptotic process, perhaps as an agglutinating platform for the apoptotic machinery. However, later difficulties with control prevent the replication of these experiments. Thus, we have yet to reach a decisive conclusion.

I hope that through these selected applications of ultrafast laser at OCI, I have stirred your interest in the technology. I hope you will adopt it into your own toolset in

the course of solving scientific problems. For your reference, the publications and

patents that resulted from the work presented in this thesis are shown in Table 1.1.

Table 1.1. Published and pending manuscripts and patent that resulted from the work presented in this thesis in chronological order.

#	Type	Description
1	Publication	**Ke K**, Hasselbrink EF Jr, Hunt AJ. "Nanofabrication with Ultrafast Lasers at Critical Intensity" *Proc. SPIE*. 2005 Mar; 5714:53-62.
2	Publication	**Ke K**, Hasselbrink EF Jr, Hunt AJ. "Rapidly Prototyped Three-Dimensional Nanofluidic Channel Networks in Glass Substrates" *Anal Chem*. 2005 Aug 15; 77(16):5083-8.
3	Patent Application	Hunt AJ, Hasselbrink EF Jr, Meyhofer E, **Ke K**. "Method for Forming Nanoscale Features and Structures Produced Thereby" Application #20050064137.
4	Publication	Uram JD, **Ke K**, Hunt AJ, Mayer M. "Label-Free Affinity Assays by Rapid Detection of Immune Complexes in Submicrometer Pores" *Angew Chem Int Ed Engl*. 2006 Mar 27; 45(14):2281-5.
5	Publication	Uram JD, **Ke K**, Hunt AJ, Mayer M. "Submicrometer Pore-Based Characterization and Quantification of Antibody-Virus Interactions" *Small*, 2006, 2, 967-972.
6	Patent Application	Mayer M, Uram JD, **Ke, K**, Hunt AJ. "Use of resistive-pulse sensing with submicrometer pores or nanopores for the detection of the assembly of submicrometer or nanometer sized objects". Application #11671171.
7	Publication	Uram JD, **Ke K**, Mayer M. "Noise and Bandwidth of Current Recordings from Submicrometer Pores and Nanopores" *Small*. Submitted.
8	Publication	**Ke K**, Cheng J, Hunt AJ. "Reduction of Polar Ejection Forces Increases Chromosome Oscillation Amplitude and Revealed Unexpected Distribution of Polar Ejection Forces" *Cell*. Submitted.
9	Publication	**Ke K**, Waite AL, Cheng J, Richards N, Hunt AJ, Gumucio DL.

		"Structural Knockout of an ASC Speck Rescues Cells from Apoptosis; the Speck Is a Platform for Apoptosis" Manuscript in preparation.

References

Du,D., X.Liu, G.Korn, J.Squier, and G.Mourou. 1994. Laser-Induced Breakdown by Impact Ionization in Sio2 with Pulse Widths from 7 Ns to 150 Fs. *Applied Physics Letters* 64:3071-3073.

Du,D., J.Squier, R.Kurtz, V.Elner, X.Liu, G.Gutmann, and G.Mourou. 1995. Damage threshold as a function of pulse duration in biological tissue. *In* Ultrafast Phenomena IX. P.F.Barbara, editor. Springer, New York. 254-6.

Joglekar,A.P., H.Liu, G.J.Spooner, E.Meyhofer, G.Mourou, and A.J.Hunt. 2003. A study of the deterministic character of optical damage by femtosecond laser pulses and applications to nanomachining. *Applied Physics B-Lasers and Optics* 77:25-30.

Joglekar,A.P., H.H.Liu, E.Meyhofer, G.Mourou, and A.J.Hunt. 2004. Optics at critical intensity: Applications to nanomorphing. *Proceedings of the National Academy of Sciences of the United States of America* 101:5856-5861.

Ke,K., E.F.Hasselbrink, and A.J.Hunt. 2005. Nanofabrication with ultrafast lasers at critical intensity. *Proc. SPIE* 5714:53-62.

Ke,K., E.F.Hasselbrink, and A.J.Hunt. 2005. Rapidly prototyped three-dimensional nanofluidic channel networks in glass substrates. *Analytical Chemistry* 77:5083-5088.

Li,Y., K.Itoh, W.Watanabe, K.Yamada, D.Kuroda, J.Nishii, and Y.Y.Jiang. 2001. Three-dimensional hole drilling of silica glass from the rear surface with femtosecond laser pulses. *Optics Letters* 26:1912-1914.

Liu,X., D.Du, and G.Mourou. 1997. Laser ablation and micromachining with ultrashort laser pulses. *Ieee Journal of Quantum Electronics* 33:1706-1716.

Loesel,F.H., M.H.Niemz, J.F.Bille, and T.Juhasz. 1996. Laser-induced optical breakdown on hard and soft tissues and its dependence on the pulse duration: Experiment and model. *Ieee Journal of Quantum Electronics* 32:1717-1722.

Marcinkevicius,A., S.Juodkazis, M.Watanabe, M.Miwa, S.Matsuo, H.Misawa, and J.Nishii. 2001. Femtosecond laser-assisted three-dimensional microfabrication in silica. *Optics Letters* 26:277-279.

Pronko,P.P., S.K.Dutta, J.Squier, J.V.Rudd, D.Du, and G.Mourou. 1995. Machining of Submicron Holes Using A Femtosecond Laser at 800-Nm. *Optics Communications* 114:106-110.

Schaffer,C.B., A.Brodeur, J.F.Garcia, and E.Mazur. 2001. Micromachining bulk glass by use of femtosecond laser pulses with nanojoule energy. *Optics Letters* 26:93-95.

Uram,J.D., K.Ke, A.J.Hunt, and M.Mayer. 2006. Submicrometer pore-based characterization and quantification of antibody-virus interactions. *Small* 2:967-972.

Uram,J.D., K.Ke, A.J.Hunt, and M.Mayer. 2006. Label-free affinity assays by rapid detection of immune complexes in submicrometer pores. *Angewandte Chemie-International Edition* 45:2281-2285.

Venkatakrishnan,K., B.Tan, P.Stanley, and N.R.Sivakumar. 2002. The effect of polarization on ultrashort pulsed laser ablation of thin metal films. *Journal of Applied Physics* 92:1604-1607.

Vogel,A., S.Busch, and U.Parlitz. 1996. Shock wave emission and cavitation bubble generation by picosecond and nanosecond optical breakdown in water. *Journal of the Acoustical Society of America* 100:148-165.

CHAPTER 2

LASER-INDUCED OPTICAL BREAKDOWN

2.1. Overview of the Laser-Induced Optical Breakdown

Ultrafast femtosecond laser-induced optical breakdown in transparent dielectric is a nonlinear process where upon reaching a threshold, plasma forms and causes permanent damage. Our laser has a Gaussian spatial profile, where the intensity at the center of the beam is the highest. At low energy, only the center of the beam has energy higher than the breakdown threshold to create plasma. For femtosecond pulses, the plasma stays localized and its associated damages has no time to propagate (Du, 1996). Therefore, ablation size can be less the focus spot as illustrated in Figure 1.1.

2.2. The Breakdown Process

The quasifree electrons are generated by a process called avalanche ionization, proposed and demonstrated by Yablonovitch and Bloembergen in early 1970's. For long pulses, under strong electric field generated by the laser, a few free electrons in the background are sufficient to start the avalanche process. However, for ultrafast femtosecond pulses, in order for avalanche to occur, the free electron must reach a density of about $10^{18}/cm^3$. Because free electron background of dielectric is only about $10^8/cm^3$, a seeding process is required to generate the free electrons. The two major

seeding theories for short pulses are multiphoton ionization (MPI) and Zener tunneling. In MPI, energies from multiple photons are absorbed simultaneously to give the bound electron enough energy to escape thus becoming a free electron. Whereas, in Zener tunneling, the electric field from the laser distorts the atomic field to reduce potential barrier to a finite thickness, and thus electrons has increased probability of escaping the potential well and become a free electron. Figure 2.1 illustrates this concept. Fortunately for us, this seeding process when induced by sub-picosecond lasers is very consistent.
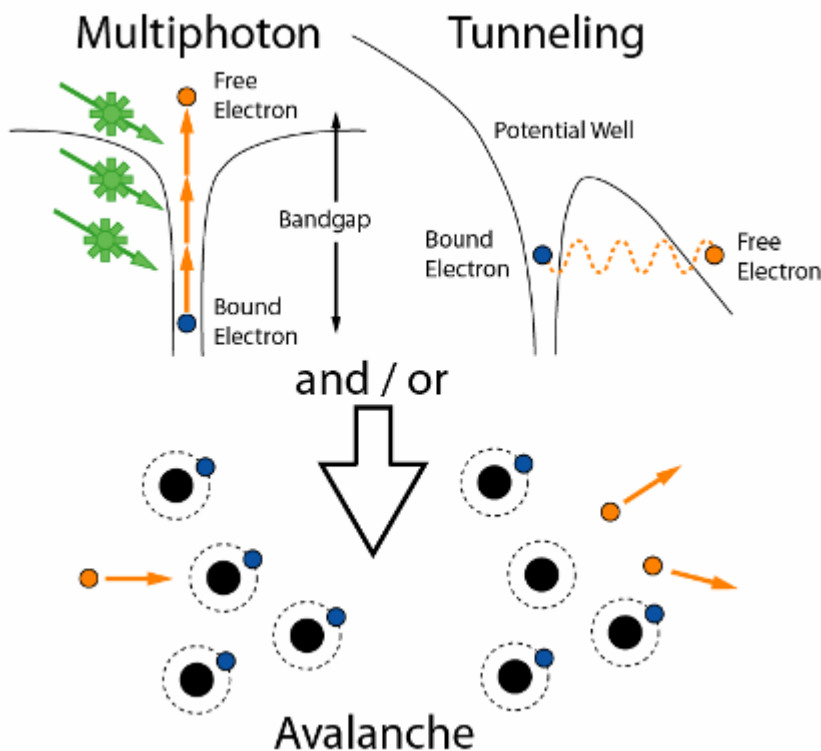
Figure 2.1. Schematics depicting the nonlinear ionization of valence electron. There are two types of seeding process: multiphoton and Zennel tunneling. In multiphoton, the simultaneous absorption of several photons by the same electron promotes the electron from the valence to the conduction band when the absorbed energy exceeds the bandgap. In Zennel tunneling, the coulomb potential well, which originally extended to infinity, is distorted by an external electric field generated by the laser. The potential is modified and became finite on one side. This gives the trapped electrons increased probability of escaping the potential well and become a free electron. Multiphoton and Zennel tunneling can occur separately or simultaneously to generate the required free electrons

to sustain avalanche ionization in which high energy free electrons free valence electrons through collision.

2.3. Breakdown Threshold

Consequentially, optical breakdown induced by ultrafast femtosecond laser is very predictable. Joglekar *et al*., (2004) reported a linear relationship between breakdown threshold and the dielectric bandgap of the material. Lower bandgap correlates with lower breakdown threshold. This means less energy is required to cause laser-induced optical breakdown in solids with lower bandgap. The breakdown threshold also depends on the wavelength of the laser. However, no polarization-dependence of breakdown threshold is observed in transparent dielectric solid.

2.4. Ablation Size

The ablation size is very deterministic because ultrafast femtosecond laser-induced optical breakdown is highly nonlinear and threshold dependent. Our laser has a Gaussian spatial profile, where the intensity at the center of the beam is the highest. Therefore, the laser energy can be attenuated to a point that only a small region of the focus spot exceeds the threshold (Figure 1.1). Thus, we were able to make 20nm holes in glass cover slip (Joglekar *et al*., 2003) which is many times smaller than the diffraction limited focus size.

The relationship between pulse energy and ablation size looks like the Gaussian profile of the laser beam turn sideways and can be modeled with the equation below:

$$D \doteq \sigma \sqrt{8\ln(E/\gamma)}$$

E - pulse energy
γ - threshold energy
σ – fitting parameter

Based on the data given in Joglekar *et al*., 2003, σ is 177±20 nm for 1053nm femtosecond laser ablation of glass focused by 0.65NA or 1.3NA objective, linearly polarized light, 163±22 nm, circularly polarized light. Breakdown threshold, γ, is given in Table 59±3 nJ (527nm, LP), 62±3 nJ (527nm, CP), 1271±75 nJ (1053nm, LP), and 1305±84 nJ (1052nm, CP).

2.5. LIOB of Biological Material

We have looked at laser-induced optical breakdown in transparent solid dielectrics such as glass. The reason is its results are applicable to biological structures such as chromosome, microtubules, cell membrane, and etc. Experimental result shows that, just like glass, ultrafast femtosecond laser can make well defined ablations consistently in both fixed cell membrane (Joglekar *et al*., 2004) and unfixed cell wall (Ke *et al*., 2005). Therefore, we believe the nonlinear characteristics of optical breakdown are similar for cellular structures as it is for glass.

2.6. Ablation Size of Biological Material

The relationship between ablation size and pulse energy is very similar to what is observed in glass. This is because optical breakdown in both glass and cellular structure are highly nonlinear and threshold dependent. Similar adjustments to the pulse energy can be made so that the ablation size is less than the focus spot. A plot of ablation size

versus pulse energy for onion cell wall and glass can be found in Figure 6.3 of Joglekar's thesis (2004). The onion cell walls have a lower breakdown threshold and a faster rise in ablation size. However, the same equation used to model the relationship between ablation size and pulse energy in glass can be adapted to model the relationship in onion cell wall. In this case, σ, the fitting parameter, is 162.7±3.76 nm and γ, the breakdown threshold, is 3.64±0.07nJ. Other cellular structures are also expected to have the same relationship but with, σ, the fitting parameter, and γ, the breakdown threshold, slightly different.

2.7. Invasiveness of LIOB

Invasiveness is evaluated in terms of the amount of collateral damage induced by the ablation. The major mechanisms are shock wave and bubble formation. The bubble, if large enough, can displace large amount of cellular structures. Shockwave, on the other hand, can induce mechanical stress in cellular structures. Bubble and shockwave formation will be looked at in more detail in the next section because it is thought to be the dominant damage mechanism (Venugopalan *et al*., 2002).

Other possible mechanisms of collateral damage are heating, photo-bleaching, reactive ions, withdrawal of air, and coating of debris. Heat must be dissipated. Un-dissipated heat can cause protein to denature. Large amount of laser energy can induce sonoluminescence and photo-bleach auto-fluorescence molecules inside of the cells. The reactive ions generated during plasma formation can modify proteins, and induce DNA damage. Air is withdrawn from the surrounding cytoplasm to fill the cavity during bubble formation. The absence of air may disrupt important reduction-oxidation

reactions. The debris is ejected and can form a thin coating on other proteins or accumulate at undesirable locations. Most of these other mechanisms are not discussed much in the literature, possibly because the energy used for ultrafast femtosecond laser microsurgery is so small that the damages caused with these mechanisms are below detectable range.

It is also quite possible that at the intensity below the breakdown threshold, the laser can still cause damage by disrupting protein-protein interaction. Many proteins dimerize with other proteins through electrostatic interactions. Apoptotic speck protein (ASC), for example, has six alpha helices in its pyrin domain (PYD). Two of which are strongly positive, while the other two, strongly negative on the surface (Liepinsh *et al.*, 2003). If the association between pyrin domains was due to charge-charge interactions, the electric field created by the laser, even when it is less than the breakdown threshold, could weaken or disrupt this interaction and cause ASC aggregates to dissolve.

2.8. Cavitation Bubble and Shock Wave Dynamics

Cavitation bubble and shock wave are often created by lasers with pulse duration longer than picosecond (Venugopalan *et al.*, 2002). The reason is that ultrafast femtosecond creates very little damage, especially near the threshold. As we will see in Chapter 3, bubble created with ultrafast femtosecond laser with pulse energy less than 10nJ are less than 1.5µm in diameter. At the pulse energy (2 to 3 nJ) typically used to ablate biological material, they are below the detection limit. Estimation of bubble size based on the equation published in Vanugopalan *et al.*, 2002 is smaller than the expected ablation size. Shockwave depends on the collapse speed of the bubble as well as the size

of the bubble. The microbubbles created with ultrafast femtosecond laser are highly damped and surprisingly long-lived. The estimated shock wave is negligisble.

We believe ultrafast femtosecond ablation of cellular components causes little bubble and shockwave formation because the majority of the pulse energy is used to form the plasma and very little is deposited after the plasma has formed. Lasers with longer pulses, on the other hand, still have plenty of pulse time left after plasma formation. Therefore, femtosecond laser causes little collateral damage when the pulse energy is near the threshold. Consequently, if a large ablation area was needed, multiple low energy pulses should be used instead of a single high-energy pulse.

2.9. Recent Applications of LIOB in Biology

Recently, ultrafast femtosecond lasers have been slowly making advances into biological research and surgery. Konig *et al*. (2001) demonstrated the capability of ultrafast femtosecond laser in altering subcellular structures by making ablations as small as 100nm in fixed human chromosomes. Subsequently in 2002, Tirlapur *et al*. demonstrated targeted transfection of CHO cells by ablating the cell membrane of selected cells while leaving others intact. Then in the same year, they ablated portions of chloroplasts, observed the pattern of cytoplasmic streaming in the targeted cells, and found no effect in cell viability and activity (Tirlapur *et al*., 2002b). Collectively, these experiments showed feasibility of using ultrafast femtosecond laser to alter subcellular structures with nanometer spatial resolution for studying cellular processes without affecting cell viability. Simultaneously in the area of medical surgery, Intralase Inc. uses ultrafast femtosecond laser for vision correction by reshaping the curvature of the cornea.

More recently, to treat presbyopia, they make subsurface micrometer size incisions in sclera (Sacks *et al*., 2002).   Ultrafast femtosecond laser will definitely become more prevalent in biological research and in surgery. In the next few chapters, we will find out about the use of ultrafast femtosecond laser in nanofluidics, mitosis, and apoptosis.

2.10. Conclusion

In summary, pulsed lasers with pulse duration shorter than a picosecond will create less collateral damage than lasers with longer pulse duration. When a laser is focused and with appropriate energy adjustment, only a small region that exceeds the material breakdown threshold will create damage and not the entire optical path. Using these two principles, we created a powerful tool to investigate the fabrication of 3D nanofluidics in glass (Chapter 3), mitosis (Chapter 4), and apoptosis (Chapter 5).

References

Du,D. 1996. Laser-induced electric breakdown in optical materials with pulse widths ranging from 55 fs to 7 ns.

Gontier,Y. and M.Trahin. 1973. Multiphoton Ionization Induced by Circularly Polarized Radiation. *Physical Review A* 7:2069-2073.

Joglekar,A.P., H.Liu, G.J.Spooner, E.Meyhofer, G.Mourou, and A.J.Hunt. 2003. A study of the deterministic character of optical damage by femtosecond laser pulses and applications to nanomachining. *Applied Physics B-Lasers and Optics* 77:25-30.

Joglekar,A.P., H.H.Liu, E.Meyhofer, G.Mourou, and A.J.Hunt. 2004. Optics at critical intensity: Applications to nanomorphing. *Proceedings of the National Academy of Sciences of the United States of America* 101:5856-5861.

Joglekar,A.P. 2004. A study of directional instability during mitotic chromosome movement.

Ke,K., E.F.Hasselbrink, and A.J.Hunt. 2005. Nanofabrication with ultrafast lasers at critical intensity. *Proc. SPIE* 5714:53-62.

Konig,K., I.Riemann, and W.Fritzsche. 2001. Nanodissection of human chromosomes with near-infrared femtosecond laser pulses. *Optics Letters* 26:819-821.

Liepinsh,E., R.Barbals, E.Dahl, A.Sharipo, E.Staub, and G.Otting. 2003. The death-domain fold of the ASC PYRIN domain, presenting a basis for PYRIN/PYRIN recognition. *Journal of Molecular Biology* 332:1155-1163.

Lompre,L.A., G.Mainfray, C.Manus, and J.Thebault. 1977. Multiphoton Ionization of Rare-Gases by A Tunable-Wavelength 30-Psec Laser-Pulse at 1.06 Mum. *Physical Review A* 15:1604-1612.

Sacks,Z.S., R.M.Kurtz, T.Juhasz, and G.A.Mourau. 2002. High precision subsurface photodisruption in human sclera. *Journal of Biomedical Optics* 7:442-450.

Tirlapur,U.K. and K.Konig. 2002. Cell biology - Targeted transfection by femtosecond laser. *Nature* 418:290-291.

Tirlapur,U.K. and K.Konig. 2002. Femtosecond near-infrared laser pulses as a versatile non-invasive tool for intra-tissue nanoprocessing in plants without compromising viability. *Plant Journal* 31:365-374.

Venugopalan,V., A.Guerra, K.Nahen, and A.Vogel. 2002. Role of laser-induced plasma formation in pulsed cellular microsurgery and micromanipulation. *Physical Review Letters* 88.

CHAPTER 3

RAPIDLY-PROTOTYPED THREE-DIMENSIONAL NANOFLUIDIC CHANNEL NETWORKS IN GLASS SUBSTRATES

3.1. Introduction

Complex microfluidic devices are of broad interest for basic research and have far-reaching applications including diagnostics, chemical analysis, sensors, drug discovery, and micro-reactors. Efforts to produce highly complex and high-density microfluidic devices capable of generalized chemical processing are challenged by space limitations and the inability to cross two planar fluidic channels without mixing. Yet, most microfabrication methods are inherently planar and few are capable of submicrometer dimensions. To date, the most complicated devices have relied on multilayer soft lithography using poly(dimethylsiloxane) (PDMS) and other polymeric materials (Unger *et al*., 2000). While these devices have intriguing possibilities, the limitations of PDMS (limited solvent resistance, leaching, protein adsorption, inability to contain high pressures) prevent adaptation to a variety of desirable analytical applications. Although silica glass has long been a "gold standard" substrate for analytical chemistry, there is considerable difficulty associated with producing multilayer all-glass micro-devices with reasonable device yield.

We present a means to rapidly prototype three-dimensional submicrometer-diameter channels in glass. During machining, glass is removed by inducing optical breakdown with a focused femtosecond pulsed laser. The machining is direct, requires no post-processing, and can produce extremely long, deep channels in a substrate when nanomachining is performed under fluids. This is possible because microbubbles produced at the site of optical breakdown gently propel fluid-entrained debris away from the machining site, rather than causing collateral damage from shock waves or violent collapse commonly associated with laser-induced cavitation bubbles (Brujan *et al.*, 2002; Tong *et al.*, 1999).

This technique allows for rapid art-to-part production of micro-/nanofluidic devices with arbitrary 3D conduit geometries; furthermore, glass offers a number of advantages over most polymers used in rapid prototyping of microfluidics. Glass is the standard for a wide variety of analytical applications due to its relative inertness, ability to withstand high pressures and organic solvents, hydrophilicity, low adsorption, and long history of well-characterized surface derivatization chemistries. High-pressure liquid chromatography (HPLC), patch clamping, microsequencing, and other integrated microscale analysis systems should especially benefit from this fabrication method.

Optical breakdown induced by femtosecond laser pulses is extraordinarily precise when the energy is near threshold, that is, at "critical intensity" (Joglekar *et al.*, 2004). The precision of optics at critical intensity (OCI) enables reproducible laser machining of subdiffraction limit features on surfaces (Du *et al.*, 1995; Liu *et al.*, 1997; Pronko *et al.*, 1995; Schaffer *et al.*, 2001; Venkatakrishnan *et al.*, 2002), and precision down to the nanoscale has recently been demonstrated by producing *surface* features on the order of

10 nm on a wide variety of materials (Joglekar *et al.*, 2004; Joglekar *et al.*, 2003). This

competes with the resolution of e-beam lithography but is more straightforward and less

material-specific. We hypothesized that OCI nanomachining might be able to directly

produce *subsurface* features, thereby enabling free-form 3D nanofabrication, provided a

mechanism were available for rapid debris removal.

3.2. Methods

Machining was performed using 800-fs pulses, 10-20 nJ/pulse, frequency doubled

to 527 nm, and produced by a directly diode-pumped Nd:glass, CPA laser system

(Intralase Corp., Irvine, CA) with a repetition rate of 1.5 kHz. The pulse energies were

selected for subdiffraction limit nanoscale machining, which covers energies from ~4

(the threshold for optical breakdown) to ~20 nJ. The target substrate (typically a glass

coverslip) is placed on a three-axis microscope nanomanipulation stage (Mad City Labs,

Inc., Madison, WI), as shown in Figure 3.1. Water or other fluids are brought into

contact with the side of the substrate distal to the microscope objective (NA = 1.3). The

laser is focused to a spot at the substrate-fluid interface, which is located when a single

laser pulse simultaneously forms a hole in the substrate and a bubble in the fluid. The

bubble, upon expansion, acts to remove the debris created by machining. The nanostage

moves the substrate in a preprogrammed pattern to create the different parts of a

nanofluidic channel. To machine wells, the stage moves the substrate 2 nm/step, 1200

steps/s, scanning successively deeper into the substrate until the desired depth is

achieved. This can be done with a fairly wide range of laser repetition rates and scanning

rates: we have successfully machined wells using laser pulse repetition rates ranging

from 75 to 2000 Hz, and scanning rates from 85 to 1200 steps/s. Long horizontal channels are produced by scanning the sample in a back-and-forth pattern, in 100-nm steps: 10 μm forward, and then 7 μm backward for a net forward movement of 3 μm; this is repeated until the desired length is achieved. This back-and-forth scanning promotes debris expulsion by bubbles formed in the water. Typically, a single pass using this procedure is sufficient to form an open channel, but greater uniformity can be achieved with multiple passes. A detailed description of the machining setup can be found in Ke *et al*., 2005.
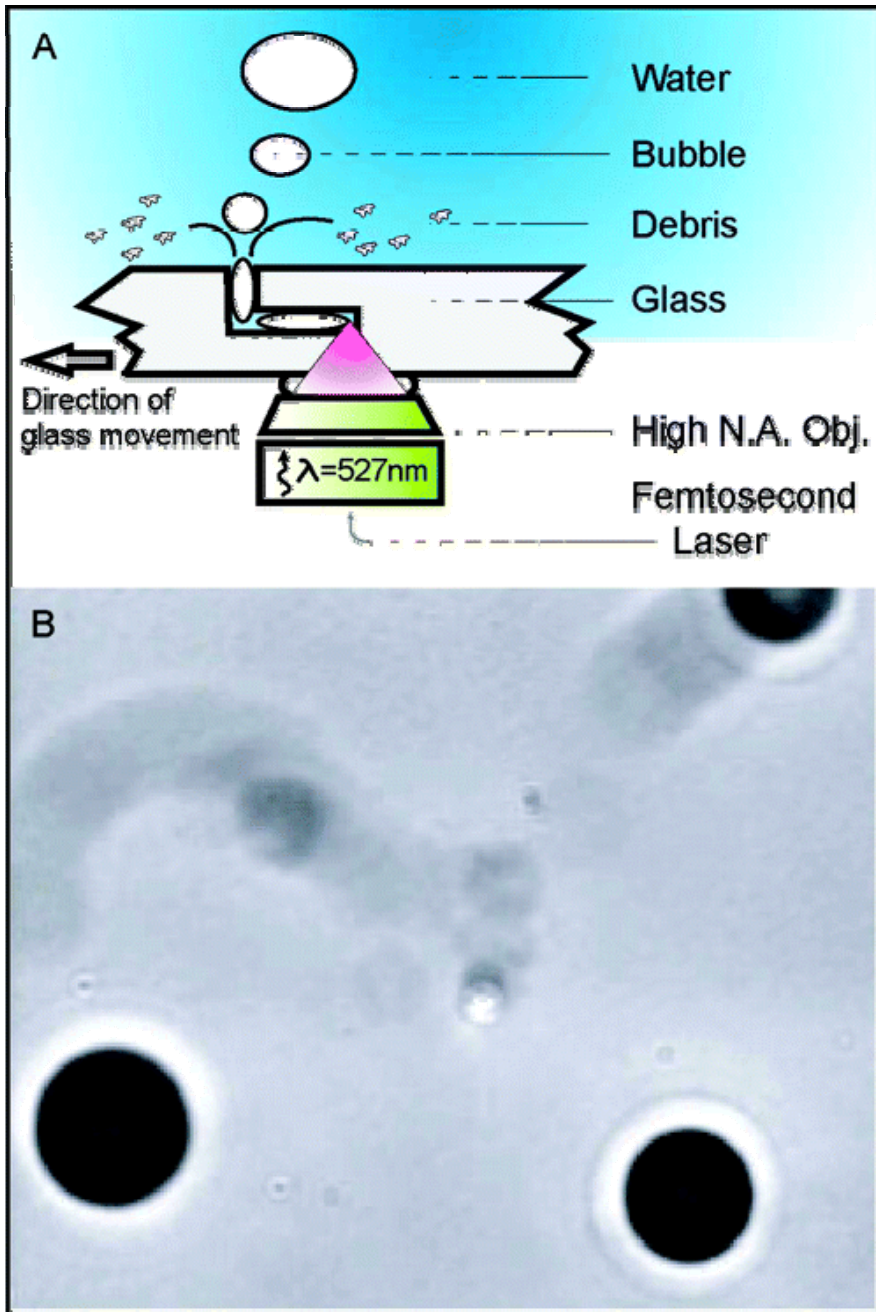
Figure 3.1. Schematic of laser nanomachining system. **(A)** Femtosecond pulses are focused through a high numerical aperture oil-immersion objective onto the target substrate (Joglekar *et al*., 2003). The substrate is immersed in water and scanned through the laser focus with a nanopositioning stage. **(B)** Bright-field micrograph shows bubbles formed as a part of the machining process (dark spots), which carry the debris away from the machining spot (bright spot slightly below the center).

3.3. Results and Discussion

Previous attempts at microscale machining have resulted in channels of several micrometers in diameter that are filled with debris (Li *et al*., 2001; Marcinkevicius *et al*., 2001), which can be cleared to produce channel diameters as small as ~10 µm by ~1 hour HF etch (Marcinkevicius *et al*., 2001). Debris can be cleared from larger channels (~30-50 um) by ultrasonic waves (Hwang *et al*., 2004). We encountered the same problem in air, but found that by submersing the glass target in water and tightly focusing the laser (see Figure 3.1), debris-free, submicrometer channels could be machined directly. In contrast, 4-7-µm-diameter channels produced under water using a less tightly focused laser retain extensive visible debris (Li *et al*., 2001). By scanning a glass target through the laser focus, complex 3D structures can easily be produced; especially remarkable is the production of channels of extremely small diameter (<700 nm) and relatively long length (>200 µm), yet free of debris and which readily convey fluid flow (Figure 3.2).
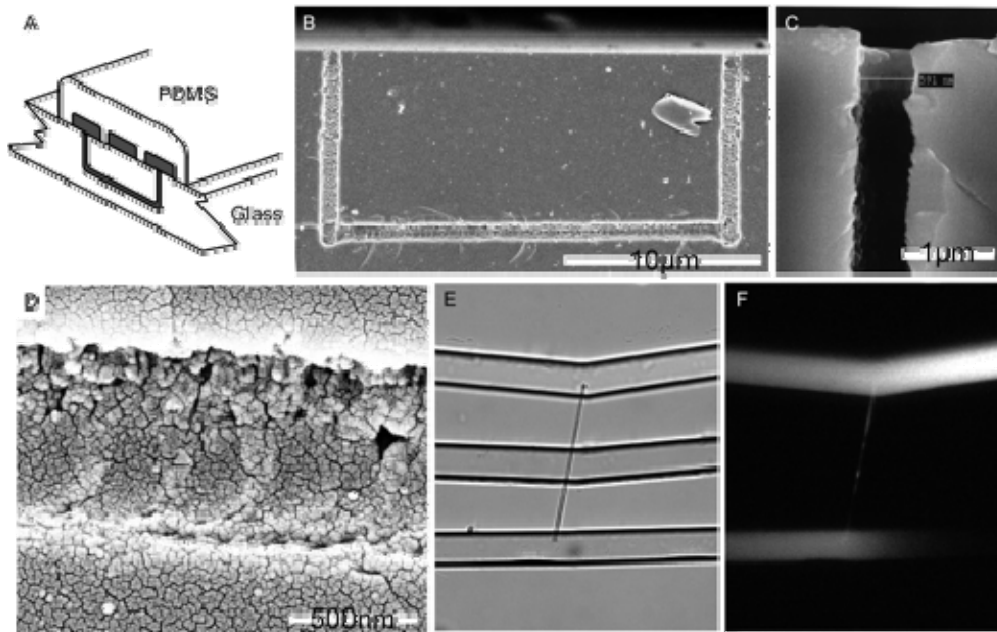
Figure 3.2. Nanofluidic jumper. The problem of joining two streams separated by a middle stream without mixing is solved by machining a nanoscopic U-shaped channel traversing underneath the middle stream. **(A)** Schematic of the nanojumper. **(B)** SEM of a cross section of the jumper. Cross-section view was obtained by simply manually snapping the glass in two after "scoring" the top surface with the laser. Scale bar, 10 μm. **(C)** Closeup of another channel machined using smaller steps between pulses to produce a smoother surface. Scale bar, 1 μm. **(D)** Closeup of a segment of the nanojumper showing the roughness of the inner channel surface. Scale bar, 500 nm. **(E)** Transmitted light microscopy image of the jumper (top view). Nanojumper length is 117 μm. **(F)** Fluorescence microscopy image of the jumper showing fluid flow from the top channel to the bottom channel without contaminating the fluid in the middle channel. Fluid flow is produced by electroosmosis using a potential of a few volts.

Since machining depends on expulsion of debris from the nanochannels, the dynamics of expanding bubbles formed during the machining process is critical. In classical studies on laser-generated cavitation, it has been shown that bubbles can collapse violently, and if near a solid surface, this collapse can produce spalling or debris pulverization by shock waves (Rayleigh, 1917) and reentrant jets (Benjamin and Ellis, 1966; Lauterbo, 1974). Such cavitation bubbles typically have maximum diameters d_{max} ~ 1 mm and collapse times τ_c ~ 2-300 μs, resulting in supersonic speeds at the bubble

wall during the final moments of collapse. These studies, however, have been conducted using lasers with 6 orders of magnitude more pulse energy (>10 mJ) than in our experiments (~18 nJ) (Brujan *et al*., 2002; Noack and Vogel, 1998; Shaw *et al*., 2000; Vogel *et al*., 1996; Vogel *et al*., 1999), resulting in relatively high Reynolds number bubbles ($Re = 10^2$ - 10^6). In contrast, video of bubbles created in water by our tightly focused, but very low-energy femtosecond pulses reveals bubbles that are 3 orders of magnitude smaller (d_{max} = 1-5 µm) and that persist ~2 orders of magnitude longer, (for energies used during machining, collapse time τ_c ~ 10-50 ms (Figure 3.3)). This counterintuitive observation - lower energy bubbles are longer lived - results in characteristic collapse speeds (~1 mm/s), far below sonic. This is far below collapse speeds at which spalling is observed, and we confirmed experimentally by producing bubbles just 1 µm above a glass surface, spalling does not contribute to the machining process.
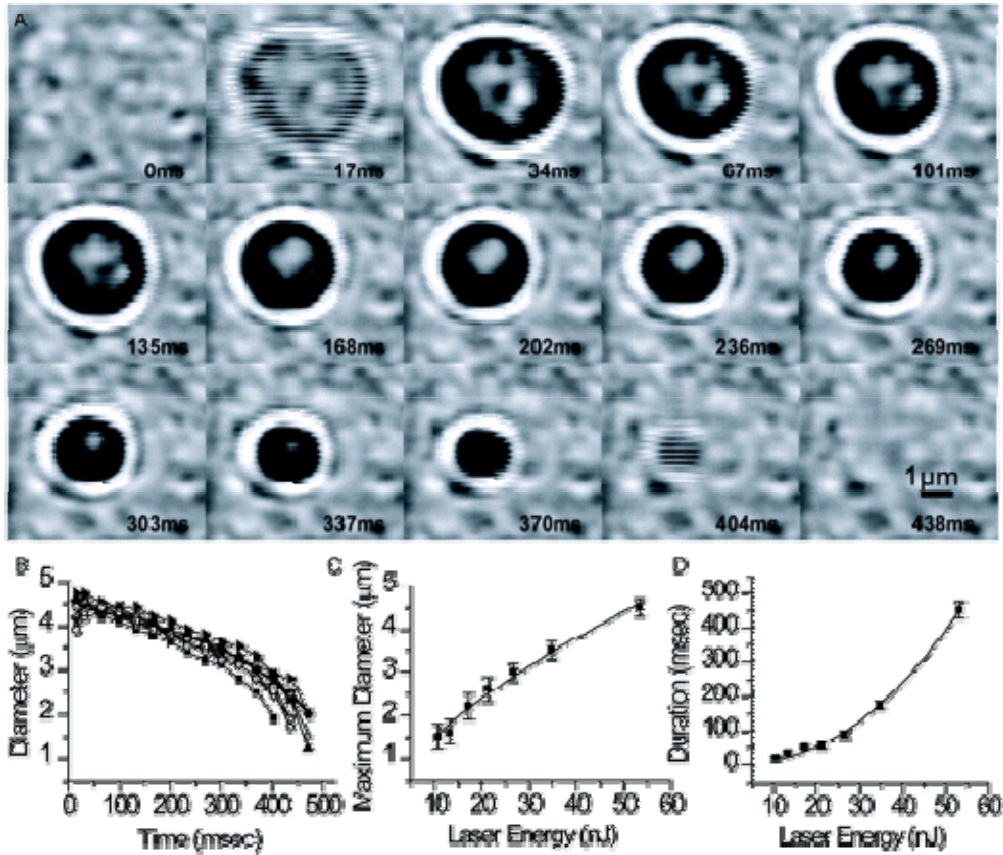
Figure 3.3. Low-energy femtosecond laser-induced bubble dynamics. Bubbles created by tightly focused, femtosecond laser near critical intensity differ significantly from classical laser cavitation bubbles; they are smaller and longer in duration. The expected collapse speed is far below sonic; thus collateral damage from bubble is eliminated. Bubbles were created in a vented chamber ~2.5 µm deep, which was fabricated using OCI nanomachining, so larger bubbles encounter the ceiling and the floor of the chamber. **(A)** Frame-by-frame morphology of a bubble created with a single laser pulse of 53.3 nJ. Scale bar, 1 µm. **(B)** Diameter versus time for 10 different bubbles, each generated with single laser pulse of 53.3 nJ. **(C)** Maximum bubble diameter versus laser energy ($n = 10$). **(D)** Bubble duration versus laser energy ($n = 10$). Rayleigh bubble scaling implies $d^5_{max}/\tau^2 \sim (16\pi/\rho)E$ Least-squares power law fits to the data in (C) and (D) show $d_{max} \sim E^{0.70}$ and $\tau \sim E^{1.9}$, respectively; thus $d^5_{max}/\tau^2 \sim E^{0.91}$. We note that the entire lifetime of a bubble, on the order of 100 ms, is long enough to allow bubbles to be further inflated by subsequent shots at the 1.5 kHz repetition rate used for machining. The resulting bubbles can be large enough that they are extruded from the mouth of a channel if it is less than a few hundred micrometers from the site of optical breakdown. We find that using multiple passes, sweeping the laser back and forth across the region to be machined away, allows fluid to refill into the cavity once these large bubbles have been initially created.

These small, highly damped, long-lived bubbles exhibit many characteristics of classical theory for bubble behavior. Purely inviscid Rayleigh analysis for bubble collapse predicts bubble lifetime $\tau_{c,Ray} \sim (3\rho/8\Delta P)^{1/2}d_{max}$. Although the viscous term in the Navier-Stokes equations disappears in a purely radial flow, a net viscous force can still occur at the interface, as captured in the Rayleigh-Plesset equation (Chapman and Plesset, 1972; Young, 1999; Yu *et al.*, 1995). Asymptotic and numerical solutions (Figure 3.4) show the time scale for collapse at low Reynolds number, *Re*, scales approximately as $\tau_c \sim \tau_{c,Ray}/Re$ for $Re \ll 1$. Collapse times and maximum diameters of bubbles produced at the energy ranges used for nanoscale machining are shown in Figure 3.3, and indeed, we find collapse times on the order of 10,000 times longer than $\tau_{c,Ray}$ at $Re \sim 10^{-4}$. Interestingly, the bubbles also show reasonable agreement with at least one result from classical dimensional analysis for *inviscid* adiabatic spherical bubbles: $d^5_{max}\rho$ $/\tau^2 E = \Pi$, where Π is a universal constant. In our experimental data (Figure 3.3), $d_{max} \sim$ $E^{0.70}$ and $\tau \sim E^{1.9}$; therefore, $d^5_{max}/\tau^2 \propto E^{0.91}$. Deviation of the exponent from unity may be attributed to the proximity of the walls during the experiments, which were performed in a chamber $\sim$2.5 μm deep to keep the bubbles in the focal plane. However, taking the constants of proportionality into consideration, the data also illustrate that the apparent mechanical energy of the bubble is several orders of magnitude less than the absorbed energy (absorbed energy is roughly 10% of pulse energy, Vogel *et al.*, 1999). This is certainly, in large part, due to the dominance of viscous dissipation and heat loss for these very low Reynolds and Peclet number ($Pe \sim 10^{-4}$) bubbles, as well as the energy required for phase change. In short, it seems likely that (a) bubble growth and collapse do not directly modify the glass substrate through jet formation and (b) the bubble

mechanical energy is largely diffused away by thermal conduction. Thus, machining is

aided by an ideal regime of gently expanding bubbles that propel away debris without

causing spalling damage associated with violent collapse.
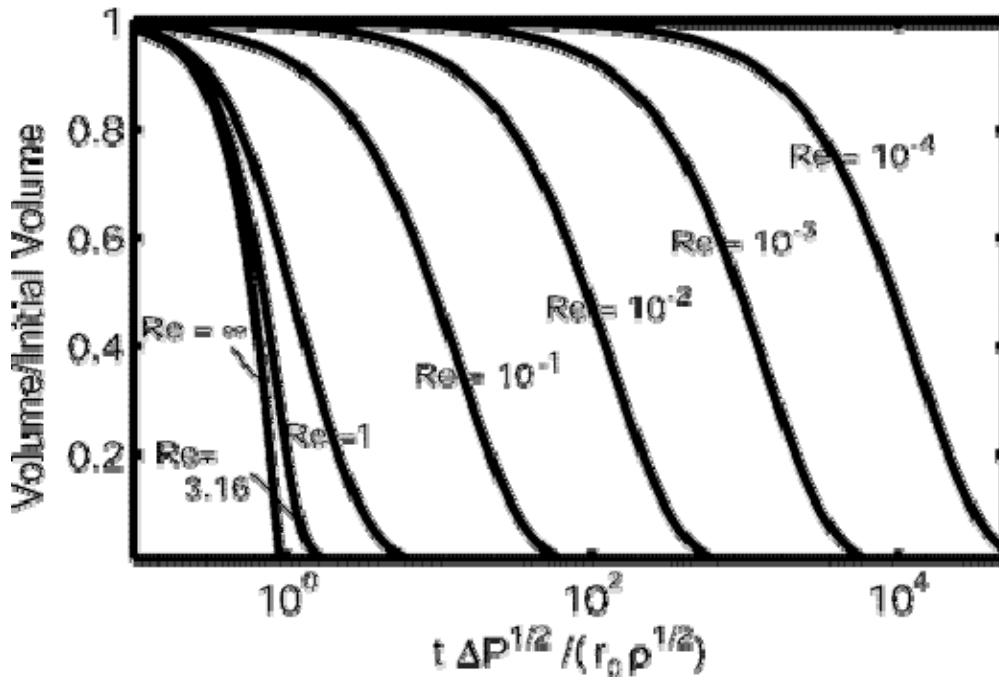
Figure 3.4. Viscous bubble collapse. Curves above are solutions for the Rayleigh-
Plesset equation, which can be written in dimensionless form as $R(d^2R)/dt^2) +
(3/2)(dR/dt)^2 + (1/Re)(4/R)(dR/dt) + 2\gamma/R + 1 = 0$, where R is the bubble radius
normalized by initial radius R_0. $Re = \rho R_0 U_c/\mu$, where ρ is liquid density, $U_c = (\Delta P/\rho)^{1/2}$ is
the inviscid characteristic collapse speed, and μ is the dynamic viscosity. The parameter
$\gamma = \sigma/R_0 \Delta P$, where σ is the surface tension and ΔP is excess pressure compared to the
pressure far away from the bubble, is usually small. For the calculations above, γ is set to
zero to show that the time scale for collapse grows larger as Re^{-1}: note the logarithmic
axes, and linear spacing of curves as Re is decreased by successive decades.

We note that the entire lifetime of a bubble, on the order of 100 ms, is long

enough to allow bubbles to be further inflated by subsequent shots at the kilohertz

repetition rate used for machining. The resulting bubbles can be large enough that they

are extruded from the mouth of a channel if it is less than a few hundred micrometers

from the site of optical breakdown, thus completely ejecting debris from the channels to further aid the machining process. However, it is possible that as repetition rates are increased eventually fluids may be entirely excluded from the machining site, thereby decreasing the efficiency of debris removal. But for the kilohertz pulse rates used here, we find the channels remarkably free of debris.
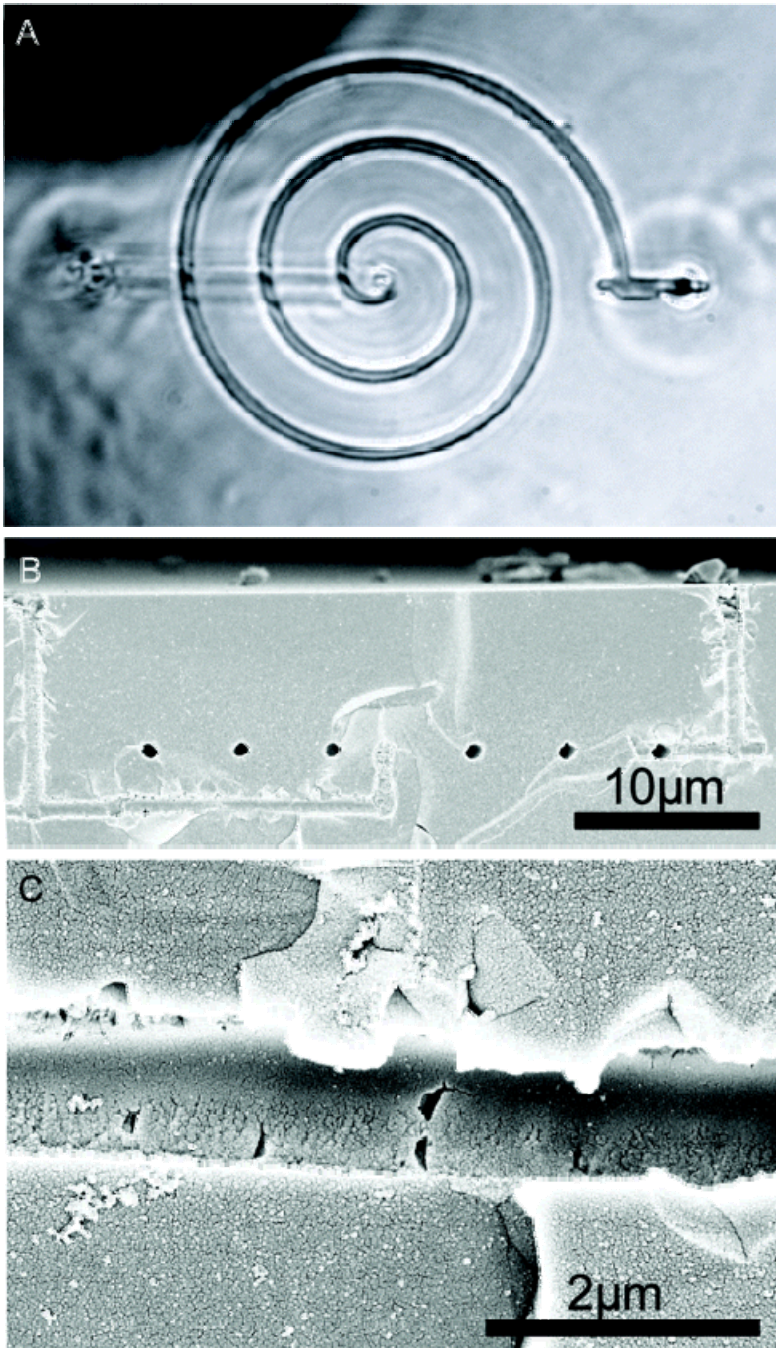
Figure 3.5. Spiral. A spiral channel demonstrates the ability to produce long channels in a small space for separation, for hydrodynamic flow resistance, or to allow mixing. **(A)** Transmitted light microscopy image of the spiral. The spiral was machined at 18 nJ/pulse to produce a channel diameter of 900 nm and length of 143 μm. **(B)** SEM cross section of the spiral showing it is free of debris. Scale bar, 10 μm. **(C)** Closeup of a segment of the spiral showing the roughness of the inner channel surface. Scale bar, 2 μm.

Applying this "submerged" OCI nanomachining method, we address three major challenges in microfluidics. First, in contrast with planar photolithographic techniques, 3D machining enables construction of out-of-plane jumpers, allowing fluids to cross paths without mixing as shown previously in Figure 3.2. The jumper was produced with just ~3 min of laser exposure, and more rapid machining is likely possible using a higher repetition rate laser. The surface roughness within the channel is of the order 10 nm (Figure 3.2D). This can be improved by decreasing the speed that the target is scanned (e.g., Figure 3.2C), presumably due to decreased separation of the well-differentiated regions of damage produced by subsequent shots (Joglekar *et al.*, 2004). While this achievement is conceptually simple, it overcomes an important practical limitation to the device density possible with single-layer glass-substrate microfluidics. In Figure 3.5, we demonstrate the ability to machine arbitrary channel geometries and to produce long channels in a small space for chromatographic separations, hydrodynamic resistance, or to allow mixing. The spiral channel shown also demonstrates that multiple layers of channels may be constructed above or below each other; this was accomplished by machining the uppermost channels first, so that refraction from machined surfaces does not interfere with the focusing of the laser.
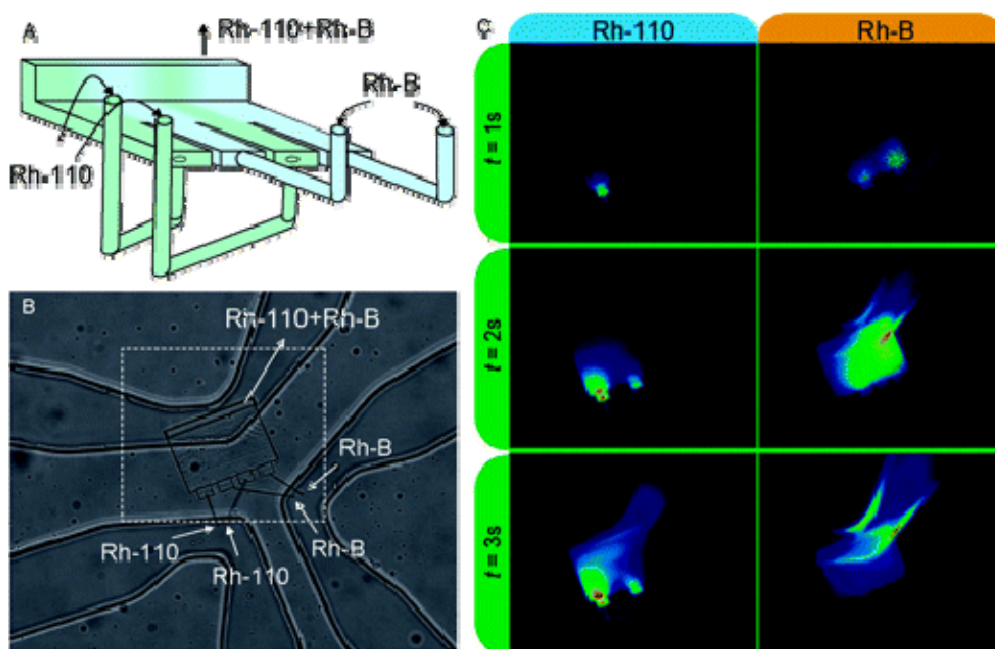
Figure 3.6. Mixer. **(A)** Concept: As predicted by diffusion theory, since mixing time scales with the second power of the diffusion distance, the mixing time of fluids can be enhanced by interleaving flows, but interleaving requires a three-dimensional channel network. **(B)** Transmitted light microscope image of device. The three chevron-shaped channels are microfluidic channels (cast in PDMS, placed atop a glass coverslip) that serve as reservoirs. Fluids are drawn through laser-machined nanochannels and mixed in the wide, flat, rectangular cavity shown. The large rectangular mixing cavity (65 μm × 52.5 μm) is fabricated using the same femtosecond laser machining process. A 10-V potential is applied to the chip reservoirs creating the flows (arrows) via electroosmotic flow. **(C)** Proof of concept: A time series of images (chip is powered at $t = 0$) showing mixing of fluorescent dyes Rhodamine-110 (Rh-110) and Rhodamine-B (Rh-B). Dyes appear first at the left and right sides of the cavity because these are the shortest paths from the reservoirs. We note that normally, epifluorescent imaging of passive dyes overestimates mixing due to line-of-sight integration of signal; in the present case, this is expected to be minimal due to the shallowness of the cavity (height, ~500 nm; width, ~65 μm).

In Figure 3.6, we demonstrate a simple 3D mixer. Mixing fluids at the micro- and nanoscale is paradoxically difficult, since it depends on relatively slow diffusion across laminar flows, due to the inability to create turbulence in such tiny channels. Taking advantage of the ability to produce 3D geometries (Figure 3.6A), two different fluids are

divided into four small channels that crisscross, so that the two fluids are interdigitated at the outflow of the small channels. By increasing fluid-fluid interface, and decreasing the width of each stream, mixing is substantially accelerated since mixing time scales with the second power of the diffusion distance.

These results demonstrate the efficacy of OCI nanomachining for creating submicrometer channels in arbitrary 3D patterns in transparent dielectric materials. We have also used the same method to machine solid 3D objects such as cones, spheres, and cantilevers. OCI nanomachining of analytical devices in glass, with femtoliter fluid volumes, enables rapid art-to-part construction of micro- and nanofluidic devices with potential to dramatically accelerate development of µTAS applications such as integrated HPLC devices, microscale sensors, and integrated nanopores for patch-clamp studies of cells. This technique is also simple to use, does not require hazardous solvents, and uses laser energies that are low enough to be safely applied using standard laser safety procedures. Despite these unique capabilities, a number of avenues for research have yet to be explored, such as the nature of the surface roughness, the retention characteristics of these surfaces when coated or left uncoated, and the performance of complete integrated analytical devices such as CE, CEC, and HPLC devices. These issues will be explored in upcoming work.

References

Benjamin,T.B. and A.T.Ellis. 1966. Collapse of Cavitation Bubbles and Pressures Thereby Produced Against Solid Boundaries. *Philosophical Transactions of the Royal Society of London Series A-Mathematical and Physical Sciences* 260:221-&.

Brujan,E.A., G.S.Keen, A.Vogel, and J.R.Blake. 2002. The final stage of the collapse of a cavitation bubble close to a rigid boundary. *Physics of Fluids* 14:85-92.

Chapman,R.B. and M.S.Plesset. 1972. Nonlinear Effects in Collapse of A Nearly Spherical Cavity in A Liquid. *Journal of Basic Engineering* 94:142-&.

Du,D., J.Squier, R.Kurtz, V.Elner, X.Liu, G.Gutmann, and G.Mourou. 1995. Damage threshold as a function of pulse duration in biological tissue. *In* Ultrafast Phenomena IX. P.F.Barbara, editor. Springer, New York. 254-6.

Hwang,D.J., T.Y.Choi, and C.P.Grigoropoulos. 2004. Liquid-assisted femtosecond laser drilling of straight and three-dimensional microchannels in glass. *Applied Physics A-Materials Science & Processing* 79:605-612.

Joglekar,A.P., H.Liu, G.J.Spooner, E.Meyhofer, G.Mourou, and A.J.Hunt. 2003. A study of the deterministic character of optical damage by femtosecond laser pulses and applications to nanomachining. *Applied Physics B-Lasers and Optics* 77:25-30.

Joglekar,A.P., H.H.Liu, E.Meyhofer, G.Mourou, and A.J.Hunt. 2004. Optics at critical intensity: Applications to nanomorphing. *Proceedings of the National Academy of Sciences of the United States of America* 101:5856-5861.

Ke,K., E.F.Hasselbrink, and A.J.Hunt. 2005. Nanofabrication with ultrafast lasers at critical intensity. *Proc. SPIE* 5714:53-62.

Lauterbo,W. 1974. Laser-Induced Cavitation. *Acustica* 31:51-78.

Li,Y., K.Itoh, W.Watanabe, K.Yamada, D.Kuroda, J.Nishii, and Y.Y.Jiang. 2001. Three-dimensional hole drilling of silica glass from the rear surface with femtosecond laser pulses. *Optics Letters* 26:1912-1914.

Liu,X., D.Du, and G.Mourou. 1997. Laser ablation and micromachining with ultrashort laser pulses. *Ieee Journal of Quantum Electronics* 33:1706-1716.

Marcinkevicius,A., S.Juodkazis, M.Watanabe, M.Miwa, S.Matsuo, H.Misawa, and J.Nishii. 2001. Femtosecond laser-assisted three-dimensional microfabrication in silica. *Optics Letters* 26:277-279.

Noack,J. and A.Vogel. 1998. Single-shot spatially resolved characterization of laser-induced shock waves in water. *Applied Optics* 37:4092-4099.

Pronko,P.P., S.K.Dutta, J.Squier, J.V.Rudd, D.Du, and G.Mourou. 1995. Machining of Submicron Holes Using A Femtosecond Laser at 800-Nm. *Optics Communications* 114:106-110.

Rayleigh,L. 1917. On the pressure developed in a liquid during the collapse of a spherical void. *Phil. Mag.* 34:94-98.

Schaffer,C.B., A.Brodeur, J.F.Garcia, and E.Mazur. 2001. Micromachining bulk glass by use of femtosecond laser pulses with nanojoule energy. *Optics Letters* 26:93-95.

Shaw,S.J., W.P.Schiffers, T.P.Gentry, and D.C.Emmony. 2000. The interaction of a laser-generated cavity with a solid boundary. *Journal of the Acoustical Society of America* 107:3065-3072.

Tong,R.P., W.P.Schiffers, S.J.Shaw, J.R.Blake, and D.C.Emmony. 1999. The role of 'splashing' in the collapse of a laser-generated cavity near a rigid boundary. *Journal of Fluid Mechanics* 380:339-361.

Unger,M.A., H.P.Chou, T.Thorsen, A.Scherer, and S.R.Quake. 2000. Monolithic microfabricated valves and pumps by multilayer soft lithography. *Science* 288:113-116.

Venkatakrishnan,K., B.Tan, P.Stanley, and N.R.Sivakumar. 2002. The effect of polarization on ultrashort pulsed laser ablation of thin metal films. *Journal of Applied Physics* 92:1604-1607.

Vogel,A., S.Busch, and U.Parlitz. 1996. Shock wave emission and cavitation bubble generation by picosecond and nanosecond optical breakdown in water. *Journal of the Acoustical Society of America* 100:148-165.

Vogel,A., J.Noack, K.Nahen, D.Theisen, S.Busch, U.Parlitz, D.X.Hammer, G.D.Noojin, B.A.Rockwell, and R.Birngruber. 1999. Energy balance of optical breakdown in water at nanosecond to femtosecond time scales. *Applied Physics B-Lasers and Optics* 68:271-280.

Young,F.R. 1999. Cavitation. Imperial College Press.

Yu,P.W., S.L.Ceccio, and G.Tryggvason. 1995. The Collapse of A Cavitation Bubble in Shear Flows - A Numerical Study. *Physics of Fluids* 7:2608-2616.

CHAPTER 4

THE MAGNITUDE AND DISTRIBUTION OF POLAR EJECTION FORCES DETERMINES THE AMPLITUDE, BUT NOT SPEED, OF CHROMOSOME DIRECTIONAL INSTABILITY

4.1. Introduction

High fidelity during mitotic cell division is required to ensure each daughter cell receives a full complement of the materials necessary to sustain life. In the case of genetic material encoded in chromosomes, failure to receive the correct copy number may result in cancerous cells or genetic disease, though more often cell death. It is thus critical that the forces that guide this fundamentally mechanical process establish a high probability of proper chromosome segregation.

During mitosis, chromosome movements depend on interactions with microtubules emanating from the spindle poles. These include diffuse interactions between microtubules and the chromosome arms, and kinetochore microtubules and the kinetochores, bundles of microtubules that attach to the nucleoprotein structures located at a chromosome's primary constriction. Chromosome movements in vertebrates exhibit distinctive oscillatory movements, first described in detail by Skibbens *et al*. in 1993, and termed "directional instability". These oscillations consist of characteristic periods of persistent movement toward or away from a pole, punctuated by abrupt reversals in

direction. Directional instability has been observed across vertebrate cell lines, including newts (e.g., Skibbens *et al.*, 1993), potoroos (e.g., Khodjakov and Rieder, 1996), and humans (e.g. Levesque and Compton, 2001). In a position versus time graph, directional instability appears as a triangular wave showing roughly constant-speed chromosome movement punctuated by abrupt direction reversals. Forces and movements directed from a kinetochore toward the pole to which it is tethered are termed "poleward", and "antipoleward" refers to the direction away from this pole.

By the 1980s, mounting evidence established that poleward motion is produced primarily by tension on kinetochore microtubules, generated at the kinetochores (reviewed in Mitchison and Salmon, 1992), and by poleward flux of kinetochore microtubules (Zhai *et al.*, 1995; Mitchison, 1989; Sawin and Mitchison, 1991; Waters *et al.*, 1996). Antipoleward movements are thought to result from "polar ejection forces" (PEFs) that push the arms of chromosomes away from the spindle poles (reviewed in Rieder and Salmon, 1994). The existence of PEFs was definitively demonstrated by Rieder *et al.*'s (1986) observation that arms severed from a chromosome by laser microsurgery move away from a nearby pole, toward spindle equator. PEFs are thought to depend on interactions between spindle microtubules and the chromosome arms, with antipoleward forces generated by chromosome-bound chromokinesin motors, or by polymerizing microtubule plus ends impinging against the chromosomes (for review, Kapoor and Compton, 2002). The forces involved in chromosome movement are depicted in Figure 1.
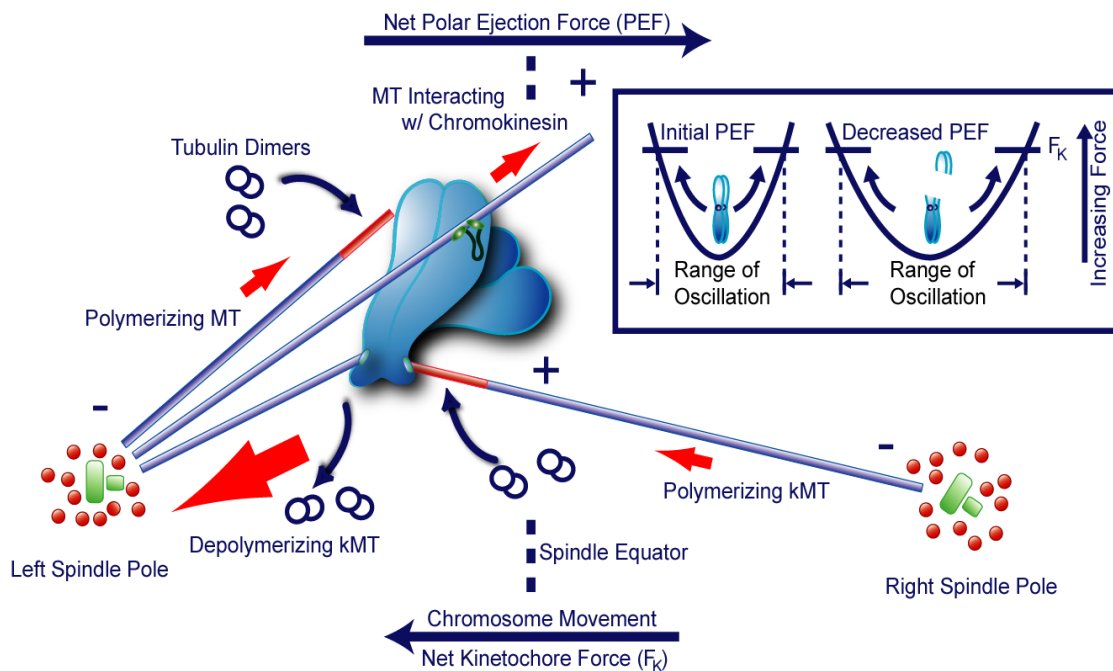
Figure 4.1. Forces driving chromosome movement. The known forces acting on a chromosome are the poleward forces on kinetochore microtubules (kMT), and polar ejection forces. The kinetochore forces consist of a pulling tension on depolymerizing kinetochore microtubules (left kinetochore) and infrequent pushing from polymerizing kinetochore microtubules (right kinetochore). The PEFs that push the arms away from a nearby pole are developed by chromokinesin motors (green and black) that move toward the plus ends of microtubules, located distal to the spindle pole. Polymerizing microtubule tips impinging against the chromosome arm could also contribute to PEFs. PEFs from each pole are oppositely directed, but the PEF from the nearer (left) pole is expected to be greater due to the higher microtubule density. The depicted chromosome will move toward the left pole if the poleward left kinetochore force exceeds the net PEF. Drawing is not to scale, and for clarity the number of polar and kinetochore microtubules is greatly underrepresented. Upper right inset models the PEF analogous to a potential well and how this predicts that a change in PEF affects chromosome movement. Confined by increasing polar ejection force pushing the chromosome away from the poles toward the spindle equator, the oscillation amplitude depends on the force required to cause reversal of the leading kinetochores. Upon severing the chromosome arm, the PEF is decreased, leading to increased oscillation amplitude.

Several models incorporate PEFs, which have been measured *in vitro* using optical tweezers at ~0.5 pN per microtubule in lateral contact with isolated CHO cell chromosomes (Brouhard and Hunt 2005), and estimated at <1.1 pN per microtubule polymerizing against a chromosome by modeling the influence of microtubules on what

were assumed to be thermal fluctuations of chromosomes in *Drosophila* embryos (Marshall *et al*., 2001). As outlined by Rieder and Salmon (1994), an appealing aspect of PEFs originating from chromosome-microtubule interactions, is that spindle microtubule density then determines the magnitude of the PEFs. Since microtubule density decreases as microtubules spread away from the spindle poles, such a mechanism provides a force that could guide prometaphase/metaphase chromosomes toward the spindle equator, where forces from opposite poles balance. One mechanism by which this could be achieved is if increasing tension at the leading kinetochore increases probability of the chromosome reversing direction (Rieder and Salmon, 1994; Joglekar and Hunt, 2002; Civelekoglu-Scholey *et al*., 2006). This leads directly to the prediction that if PEFs are reduced, the frequency of reversals will decrease, and consequently the amplitude of oscillations will increase (Figure 1 upper right inset). Conversely, the amplitude will not be decreased if PEFs do not significantly guide chromosome movements or if, as suggested by Khodjakov *et al*. (1999), PEFs guide chromosomes without influencing the force-generating state at the kinetochores and instead determine the direction of chromosome movement only when forces on the sister kinetochores are balanced (i.e. both kinetochores are in "neutral, or in balanced opposition).

The distribution of PEFs across the spindle has been modeled as an inverse square relation to the distance from the spindle poles (Joglekar *et al*., 2002; Civelekoglu-Scholey *et al*., 2006). This is expected under the simplifying assumption that all interpolar microtubules are relatively straight, and extend at least the length of the half spindle, and that the PEF is proportional to local microtubule density. The PEF is then also expected to depend on the size of a chromosome, roughly proportional to its cross-sectional area

perpendicular to the spindle axis, which establishes the target area for encounters with microtubules extending from the poles. The PEF is directed away from each pole and drops off toward the equator, where opposing PEFs are equal. Although these simplifying assumptions allow a reasonable first approximation of the PEF distribution, not all the interpolar microtubules are equal in length, and some do not even reach spindle equator (Mastronarde *et al*., 1993), so the actual force distribution may differ significantly. In addition, given the dynamic nature of microtubules, PEFs undoubtedly exhibits spatial inhomogeneities and temporal variations. Both the descriptive model proposed by Khodjakov *et al*. (1999), and the mechanistic model of Joglekar and Hunt (2002), predict that these variations will not change the defining characteristics of the chromosome motion -- directional instability manifested as approximately constant speeds and abrupt reversals of direction. Joglekar and Hunt predicts there will be an effect on that the regularity of the oscillations.

Here we examine the role of PEFs by performing experiments to alter their magnitude abruptly in Newt lung cells. Taking advantage of the precise nature of optical breakdown induced by femtosecond-pulsed (ultrafast) lasers (Joglekar *et al*., 2004; Konig *et al*., 1999), we rapidly lower the PEF by slicing off chromosome arms, thereby reducing the cross-sectional area available to interact with spindle microtubules. For laser pulse duration lower than one picosecond, the deterministic and nonlinear relation between optical breakdown and laser pulse energy allows limiting of damage to a region at the beam waist with dimensions smaller than the Gaussian diffraction-limited focus (Pronko *et al*., 1995; Joglekar *et al*., 2003). Furthermore, since femtosecond lasers enable optical breakdown with only nanoJoules of laser energy, we avoid collateral

damages due to shock waves and cavitation bubbles that may occur with longer pulses (Ke *et al.*, 2005; Juhasz *et al.*, 1999; Loesel *et al.*, 1998). We find that severing of chromosome arms increases the amplitude of chromosome oscillation without altering the defining characteristics of directional instability, thereby providing broad support of PEFs importance in directional instability, and specific support for PEFs influence on the probability of kinetochores switching states to allow reversal of chromosome movements. We discuss how a reduction in PEFs can lead to an increase in amplitude of directional instability, based on existing theories of chromosome motility during mitosis. We then calculate the distribution of PEFs based on the relationship between reduction in PEF and increased oscillation amplitude.
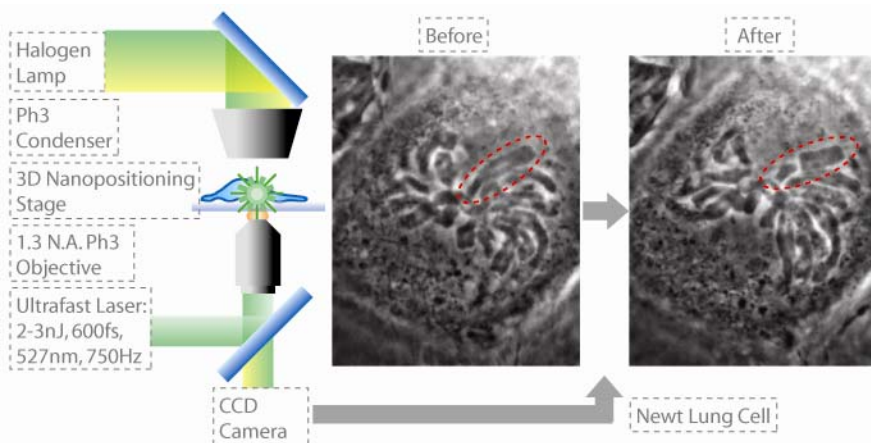
Figure 4.2. Laser microsurgery setup. An ultrafast pulsed laser is focused by a high numerical aperture objective to form a diffraction limited spot slightly exceeding critical intensity for breakdown of biological material. Under phase contrast, the chromosome appears darker than its surroundings and is thus easily visualized and targeted with a nanopositioning stage. A portion of an arm is severed by scanning the chromosome across the laser focus. The chromosome is tracked before and after ablation by time-lapse video microscopy. In the phase contrast images, left is before cutting off a piece of chromosome, the right is after.

4.2. Results

To investigate the role of PEFs in directional instability, we used a fs-pulsed laser to sever chromosome arms during mitosis in primary cultures of newt lung cells. Figure 2 illustrates the laser-ablation setup. Restricting damage to sub-diffraction nanometer-scale regions (Joglekar *et al.*, 2004; Konig *et al.*, 1999), and nanometer precision targeting allowed chromosome arms to be severed with minimal collateral damage. Chromosome movements before and after ablation were tracked by phase-contrast video microscopy, and were time-lapse recorded at 2 to 3 second intervals. Oscillation characteristics before and after the ablation were compared to determine how severing chromosomes altered directional instability.

Chromosome Selection

We tracked bi-oriented chromosomes, severed fragments of chromosome arms, and centrosomes within the mitotic spindle. For chromosome position measurements, the primary constriction was tracked since it is the most easily identified discrete region on a chromosome. Often kinetochore microtubules are difficult to discern, so we used several criteria to identify bioriented chromosomes. We assume biorientation occurs when chromosomes initially drawn toward a spindle pole suddenly shifted to the vicinity of the spindle equator. A further indications of biorientation was increased separation between sister chromatids as a chromosome undergoes directional instability, especially at direction reversals (Waters *et al.*, 1996). Although kinetochore fibers were difficult to identify near the kinetochores, fibers were frequently visible projecting from the centrosome toward a chromosome. Where possible, we picked chromosomes clearly

separated from nearby chromosomes to minimize steric interference by other chromosomes that could confound interpretation of movements. For most clearly interpretable results, we selected chromosomes that exhibited clearly discernable oscillations; this introduces some selection bias, further addressed below.

Laser surgery

Laser microsurgery to sever a chromosome arm typically takes about 30 seconds. The process begins after locating a bioriented chromosome and following its movement for a few cycles of directional instability. The chromosomes typically oscillate within 10μm of the spindle equator, with peak-to-peak amplitudes ranging from 0.8 to 7.3μm before surgery. The ultrafast laser is focused by a high numerical aperture (1.3) objective to achieve just above critical intensity for breakdown of biological material at the beam waist located on the chromosome (Figure 2). The focus is initially set at the edge of a chromosome arm, the beam is turned on, and the chromosome is moved across the focus with the nanopositioning stage. Since femtosecond laser induced damage is restricted to a subdiffraction volume in all dimensions (Joglekar *et al.*, 2003; 2004), the procedure is repeated at successive z-axis positions to sever the entire thickness of the chromosome. The entire process is then repeated once to guarantee complete separation of the chromosome arm from the rest of the chromosome. The length of the severed chromosome arms ranged from 12% to 51% of the entire length of the chromosomes. Chromosome tracking continues until anaphase. Post surgery oscillation amplitude ranged from 1.7 to 9.5μm.

Directional Instability After Surgery

A typical chromosome trace is shown in Figure 3. In this case, the chromosome is tracked for about 450 seconds prior to ablation. The first image below the trace, at 0 sec, shows the intact chromosome marked green. The chromosome arm is about 2.1μm in diameter and was severing in 28 seconds. The image at 464 second shows the chromosome immediately after the ablation. The piece of the chromosome containing the centromere is marked green, while the severed chromosome arm is blue. Initially the severed arm follows closely with the movements of the rest of the chromosome, but after about 500 seconds, the arm begins to drift away, and its movements become largely independent of the rest of the chromosome. After severing the arm, directional instability of the kinetochore-containing region of the chromosome increases in amplitude from 1.4 to 2.7μm. The amplitude does not increase for two nearby chromosomes serving as controls (see upper right inset). Note that when a chromosome reverses direction the trace is sometimes rounded rather than coming to a point as expected for abrupt reversals associated with directional instability. This is typically seen when reversals are close to the spindle equator where chromosomes are densely packed. This leads to increased probability that tracked region is pulled under another chromosome because of steric hindrance; the slight defocusing diminishes tracking precision and causes the trace to become slightly rounded.
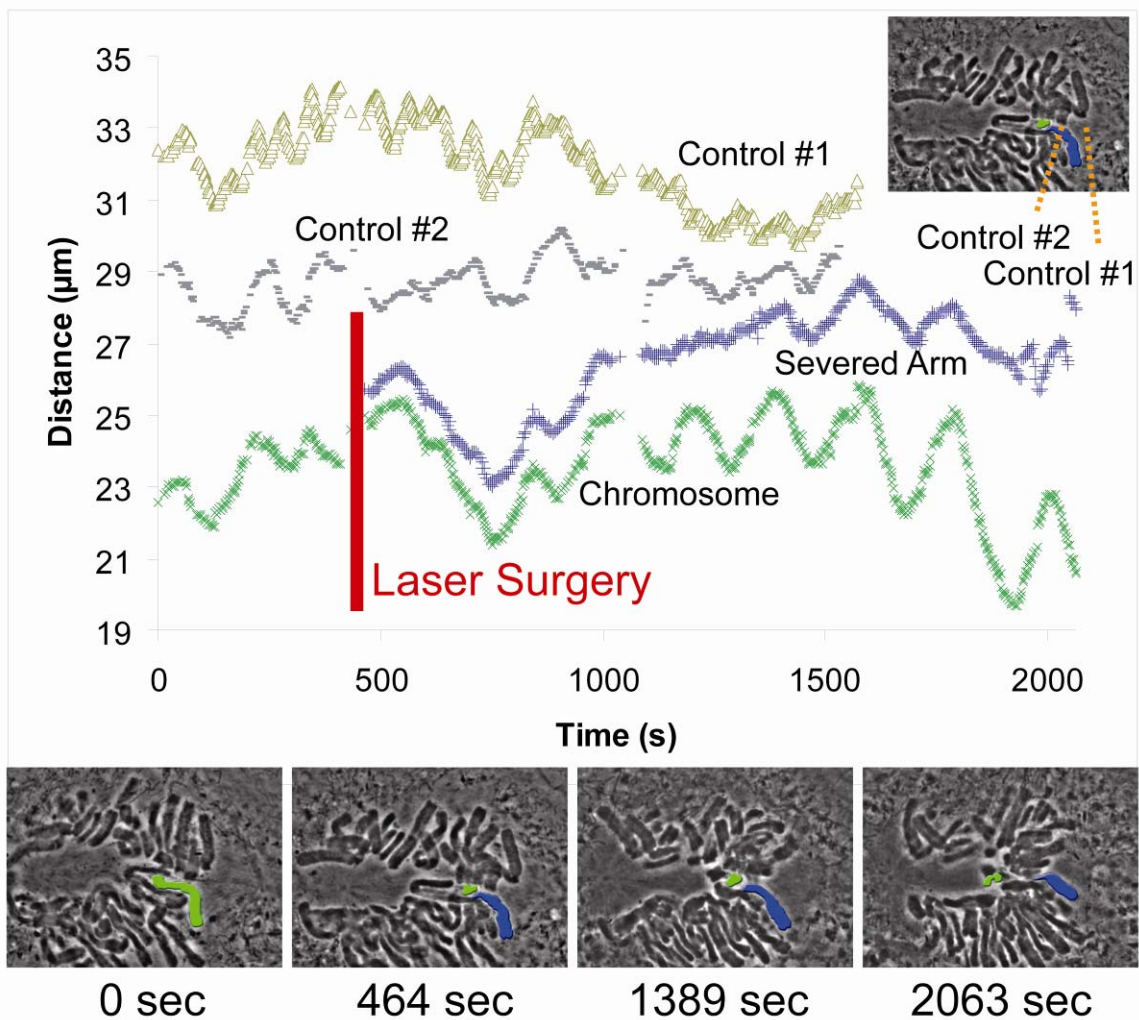
Figure 4.3. Chromosome movement relative to a reference pole before and after severing an arm. In the images and corresponding traces, blue indicates the severed arm, and green the kinetochore-containing region. Upper traces are for two nearby control chromosomes, indicated in the upper right inset. In the figures below the trace, the initially intact chromosome (first frame) oscillates at average 1.4 μm peak-to-peak amplitude. The arm is severed immediately before the second frame (464 sec). The region containing the kinetochores continues to exhibit directional instability but at higher amplitude (average 2.7 μm). The severed portion of the arm (blue) initially follows the rest of the chromosome, but by 1000 seconds, it loses synchronization with the rest of the chromosome. By 2063s, the chromosome and the severed arm have moved to opposite sides of the spindle equator. The two control chromosomes are unaffected by the surgery, and their oscillation amplitudes do not increase.

52

The speed of severed chromosomes is unchanged

We tracked the movements of 32 chromosomes before and after severing their arms. Sixteen were discarded because they proved difficult to track or because they entered anaphase before oscillations could be characterized. Of the remaining 16 chromosomes, the average speed toward the spindle equator was the same as away (30.1 ± 16.5 nm/s (mean ± s.d., n=48 runs) and 32.3 ± 18.7 nm/s (n=53 runs), respectively) and consistent with published results (Skibbens *et al.*, 1993; Khodjakov and Rieder, 1996). The overall character of direction instability was not altered when chromosomes were severed, and the speeds were unchanged: 32.9 ± 13.3nm/s (n = 75 runs) toward the spindle equator and 31.5 ± 12.9nm/s away (n = 81 runs) (Figure 4). Again, movements are constant speed and punctuated by abrupt reversals. This is consistent with the earlier observation that different sized chromosomes move at the same speed (Nicklas, 1965), and demonstrates that this is an intrinsic aspect of chromosome movement that does not depend on local spindle properties surrounding individual chromosomes. This is notable since chromosomes have been observed to adapt preferred positions in the mitotic spindle (e.g., Mosgöller *et al.*, 1991; Habermann *et al.*, 2001; Gerlich *et al.*, 2003), raising the possibility that the size of chromosomes could be compensated by the local spindle structure.
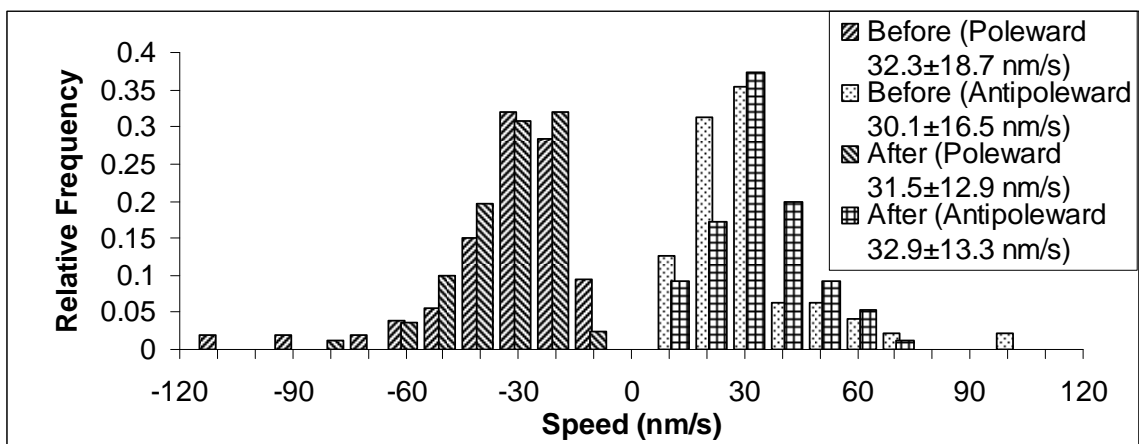
Figure 4.4. Shortening a chromosome arm does not change speed. The average speed was about 31 nm/s, and was not changed by the severing of chromosome arms. In the histogram shown, the left hash is the speed of individual poleward runs before severing the arm, right hash after; dots and grids correspond to antipoleward movements before and after severing the chromosome arm.
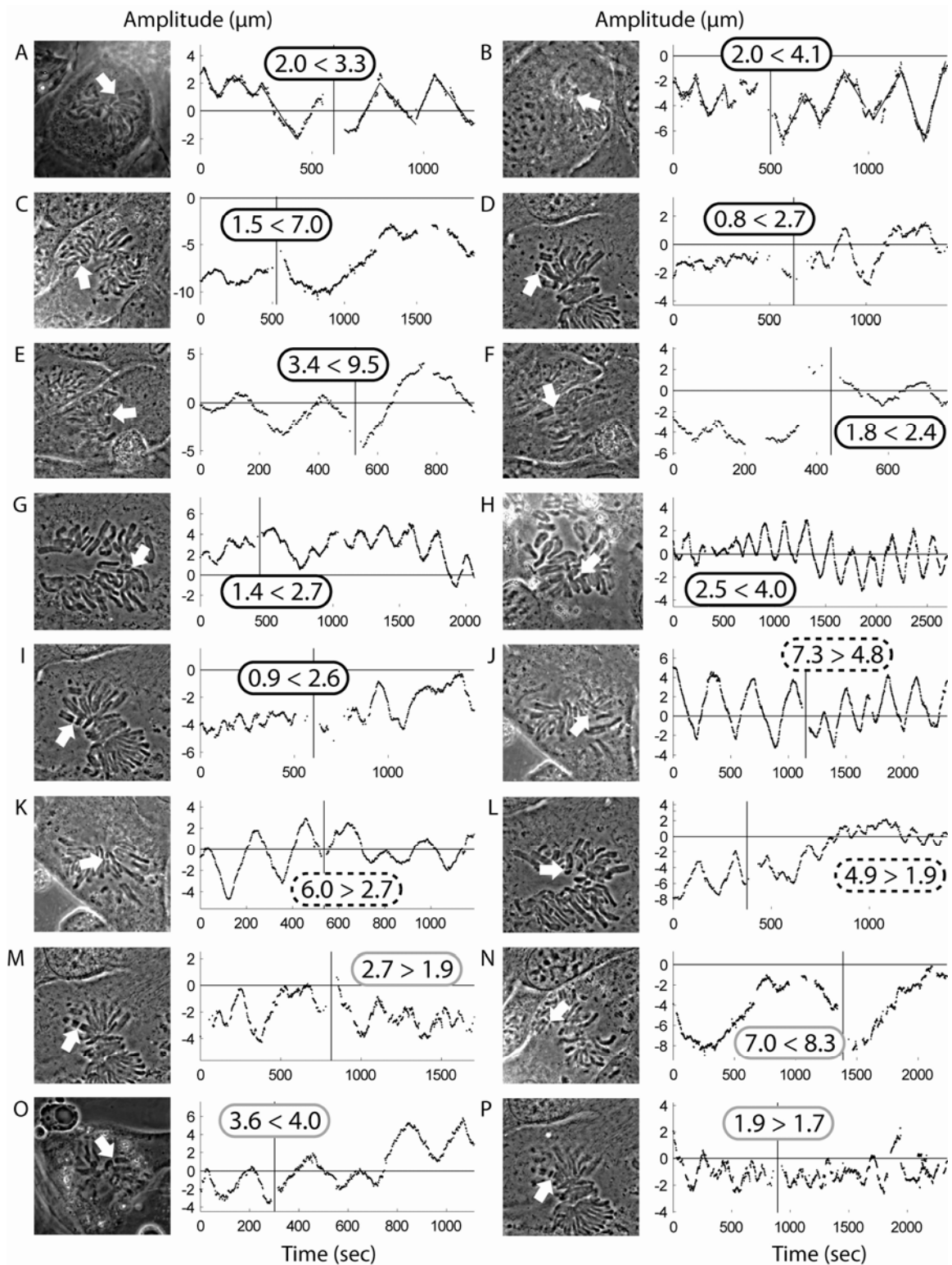
Figure 4.5. Chromosome oscillation amplitudes before and after the arms are shortened. Each panel shows a different chromosome's movements before and after surgery (indicated by the vertical line on the traces). The arrow in the phase contrast micrograph to the left of each trace indicates where each chromosome was severed. The

solid lines (Figure A & B) are linear regression fits to the data used to determine oscillation speeds and amplitudes. The number in the oval compares the oscillation amplitude before and after the ablation. Figure A-I showed significant increase in amplitude ($p<0.05$, black oval). Figure J-L showed significant decrease in amplitude ($p<0.05$, dotted oval). Figure M-P showed no significant change ($p>0.05$, gray oval).

Severing chromosome arms increases the amplitude of direction instability.

Although the defining characteristics of directional instability are not altered by chromosome ablation, the amplitude of the oscillation changes, often abruptly. The amplitude increased in nine of sixteen chromosomes after the arms were severed (Figure 5 A-I) while three showed significant decrease in amplitude (Figure 5 J-L), and four were unchanged (Figure 5 M-P). On the average, the amplitude of directional instability increases after severing the chromosome arms by 73%, in contrast to a decrease of 41% for control chromosomes (Figure 6a diamonds, only those whose observational period overlaps a surgical event of an experimental chromosome, which is used as divider for this comparison). Furthermore, most severed chromosomes follow the same rule – the longer the chromosome arm severed, the bigger the increase in amplitude (Figure 6B, explained in the next section).

Not all chromosomes showed an increase in oscillation amplitude after severing the arms, though all of them still exhibit directional instability. This may in part be explained by the slight tendency, indicated by the controls (Figure 6a diamonds), for the amplitude to decrease as mitosis progresses, but is in large explained by selection bias. Our studies necessarily focused on chromosomes whose directional instability could clearly be resolved and differentiated from the movements of other chromosomes, and these tended to be chromosomes undergoing large oscillations. Since this skews our

56

analysis towards chromosomes that initially exhibited large oscillations, there could be a general tendency for the amplitude to decrease to more typical values (i.e. regression toward the mean), offsetting the increased amplitude due to severing the arms. Indeed analysis indicates that chromosomes having very high oscillation amplitude before the ablation are less likely to show an increase in oscillation amplitude after arm shortening (Figure 6A). To compensate for this bias, we exclude data from chromosomes exhibiting initial oscillation amplitudes more than two standard deviations from the mean (1.9 ± 1.4 µm) from further analysis.
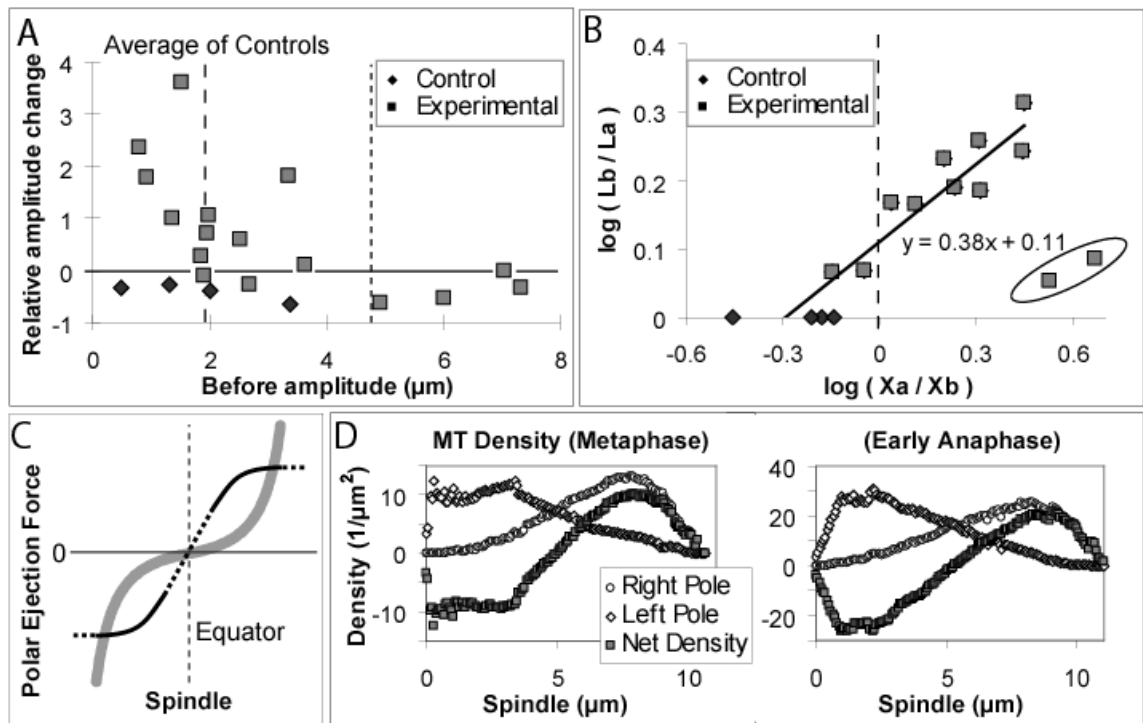
Figure 4.6. Estimation of the polar ejection force (PEF) distribution. A) The relative change in the amplitude of directional instability after severing a chromosome arm as a function of the amplitude before severing the arm (squares). Black diamonds are control chromosomes located in the same cell as an experimental chromosome, but not subject to microsurgery: in these cases the before and after amplitudes correspond to before and after severing the arm of the experimental chromosome in the same cell as the control.

The average oscillation amplitude of these 4 chromosomes and 3 other control chromosomes from cells where surgery was not performed (not shown) is 1.9 ± 1.4 µm (dashed line). The dotted line indicates 2 standard deviation away from the average at 4.7 µm. B) Estimation of the PEF distribution from the equation $F=KAx^n$ (see text for detail) for newt lung cells. The two circled outlying data points were excluded from the line fit. The slope of the line, n, is 0.4. C) From the line fit the PEF distribution is estimated to be proportional to $x^{0.4}$ (black line). The straight dotted segments indicate regions outside the range of data where reversals occur. This differs substantially from the inverse square distribution assumed in models (gray line), where the PEF is proportional to $1/(K-x)^2$, where K is half of the spindle length. Note that the line fit does not pass through zero. This is explained by the decrease in oscillation amplitude as the mitosis progresses toward anaphase, which presumably reflects increasing spindle microtubule density (e.g. Mastronarde *et al.*, 1993). D) Interpolar microtubule density at metaphase, and early anaphase of PtK1 cells, calculated from the data of Mastronarde *et al.* (1993). The polarity adjusted (net) density (squares) – the amount that the number of microtubules from one pole exceeds the other – is calculated by subtracting the right pole values (circles) from the left pole values (diamonds), and is similar to our estimation of PEF distribution (C, black line) for newt lung cells: steepest near the equator, and flattening toward the poles. The microtubule density then drops off very near the poles.

The distribution of polar ejection force (PEF)

Having established that direction reversals depend on the magnitude of PEFs, we can approximate the distribution of the PEFs from the relationship between the decrease in the length of the chromosome after severing an arm, and the resulting increase in amplitude. Assuming that the PEF increases monotonically as a chromosome moves away from the spindle equator, it can be approximated by the equation: $F=KAx^n$, where F is the PEF, K is the average PEF per unit surface area of the chromosome, A is the surface area of the chromosome, x is the chromosome displacement relative to the spindle equator, and n is an exponent describing how the PEF increases as the chromosome moves away from the spindle equator. Note that the exact distribution of the PEFs may not follow this form, but it is a useful approximation since the exponent, n, captures the general curvature of the PEF distribution: positive curvature ($n > 1$) with the PEF rising

58

increasingly steeply near the poles for, as is the case for previously used approximations (Joglekar *et al.*, 2002; Civelekoglu-Scholey *et al.*, 2006; negative curvature ($n < 1$) if the PEF increases less rapidly as the poles are approached; and $n = 1$ if the PEF increases at a constant rate. To approximate PEF, we consider the force distribution before, $F_b = KA_b x_b^n$, and after, $F_a = KA_a x_a^n$, severing the chromosome arm, denoted with subscripts before (b) and after (a). At the extremes of a chromosome's oscillation, x becomes the measured amplitudes, denoted as X_b for before and X_a for after severing the chromosome. We assume that at these locations, the PEF opposing movement of the leading kinetochore is equal to the maximum force that the kinetochore will bear before switching directions. Since we did not ablate the kinetochores or kinetochore microtubules, we assume the kinetochore forces have not changed, so $F_b = F_a = $ constant. Based on this relationship, we balance and rearrange the equations to obtain $A_b/A_a = (X_a/X_b)^n$. Because of high length to diameter ratio when approximating a chromosome as a rod with constant diameter, A_b/A_a is equal to L_b/L_a where L is the length of the chromosome. Substituting L in place of A, we obtain $L_b/L_a = (X_a/X_b)^n$, and taking the log of both sides of the equation, $\log(L_b/L_a) = n \log(X_a/X_b)$. By fitting a line to $\log(L_b/L_a)$ plotted versus $n \log(X_a/X_b)$ we solve for n (Figure 6B). We found *n* to be ~0.4, less than unity and considerably different from the value of ~ 2 for the inverse square relation used in mitotic models (Joglekar *et al.*, 2002; Civelekoglu-Scholey *et al.*, 2006).

Since the PEF has been hypothesized to depend on microtubule density (Ault *et al.*, 1991; Cassimeris *et al.*, 1994; Rieder and Salmon, 1994; Joglekar and Hunt, 2002; Brouhard and Hunt, 2005; Civelekoglu-Scholey *et al.*, 2006), we were intrigued by this low value of *n*, rather than the squared or higher relation that might be expected given 1)

the spreading of relatively straight microtubules as the distance increases from a point source, the pole, resulting in a decrease in microtubule density, and 2) the diminishing number of microtubules originating from a given pole as the equator is approached from that pole, since not all microtubule extend the entire length of the half spindle (Mastronarde *et al.*, 1993). To explain this, we examined serial electron microscopy section reconstructions of interpolar microtubules in the mitotic spindle obtained by Mastronarde *et al.* (1993). Two sets of microtubule data were provided by The Boulder Laboratory for 3-D Electron Microscopy of Cells: one for metaphase, and the other early anaphase. We calculated the density in each case by counting the number of microtubules in each spindle cross-section and dividing by the cross-section area (Figure 6D). The density of microtubules was low near the spindle poles in early anaphase and metaphase, though the density was substantially higher near one of the poles during metaphase (Figure 6D, metaphase left pole). The decreased density near the poles reflects the fact that many microtubules do not extend all the way to the pole, as noted by Mastronarde *et al.* (1993). The microtubule density then rises to a peak before dropping off a few microns from the poles. The microtubules emanating from each pole are opposite polarity, and so should result in opposing PEFs when interacting with the same chromosome. Thus by subtracting microtubule density of one pole from the other, we obtain the expected PEF distribution (squares in Figure 6D), which turns out to exhibit negative curvature moving from the equator toward the pole, consistent with our estimation of the PEFs over the region near the spindle equator where directional instability of bioriented chromosomes generally takes place. This analysis supports the hypothesis that PEFs are proportional to microtubule density, and suggests that the

60

previously used inverse square relation (Figure 6C light gray curve) fails to capture the PEF distribution because it does not account for the decreasing microtubule density near the poles, or the significant effect of microtubules that extend past the spindle equator.

4.3. Discussion

To examine the role of PEFs in mitotic chromosome movements, we perturbed the balance of forces by severing chromosome arms with an ultrafast pulsed laser. Since PEFs depend on the interaction between interpolar microtubules and chromosome arms, cutting off a piece of a chromosome's arm abruptly reduces the PEF, allowing us to examine its role in directional instability. We found that the reducing the PEF increases the amplitude of chromosome oscillations without affecting the hallmarks of directional instability – persistent speeds and abrupt reversals of direction.

PEFs push chromosomes away from the poles, moving unattached chromosomes toward the spindle equator during vertebrate mitosis (Rieder *et al*., 1986; Ault *et al*., 1991; Khodjakov *et al*., 1997). Thus PEFs are antagonistic to the poleward forces generated at the kinetochores. PEFs can be generated by the interactions of chromosome-bound motors with microtubules (Brouhard and Hunt, 2005), but it is not clear if this entirely explains PEFs since chromosomes can still congress to the spindle equator when chromokinesins are inhibited, though directional instability is suppressed (Levesque and Compton, 2001). Potentially PEFs may also arise from polymerization of microtubules into chromosome arms (reviewed in McIntosh *et al*., 2002). In either case, a reasonable expectation is that PEFs are proportional to the size of chromosome and the local microtubule density. Severing a portion of a chromosome arm reduces the

antipoleward load on the chromosome by reducing the effective interaction area between the interpolar microtubules and the chromosome. When, in this manner, we reduced the PEF load on a chromosome, the chromosome's speed was unaffected. This suggests that the speed of chromosome movements is not governed by the conventional ATP-dependent activity of motor proteins walking along the surface of microtubules. The unloaded speed of dynein, the only minus-end directed motor protein identified at the kinetochores, is about 50-fold greater than the speed of chromosome movements: the average chromosome speed is 0.03 ± 0.01 µm/s versus 1.7 ± 0.9 µm/s for dynein *in vivo*, (Kural *et al.*, 2005) or ~ 1 µm/s in vitro (King and Schroer, 2000; Nishiura *et al.*, 2004). The kinesin-family kinetochore protein CENP-E moves about 3-fold faster than chromosomes in vitro (Wood *et al.*, 1997), though this plus-end directed activity is opposite to poleward forces that are typically observed at kinetochores (Khodjakov and Rieder, 1996; Waters *et al.*, 1996).   Thus if directional instability is driven by these motors, acting in a conventional ATP-dependent manner, we expect they are working against a load approaching the force at which they stall. Since the speed of conventional ATP-dependent motor proteins decreases monotonically as the load increases (Schnitzer *et al.*, 2000; Meyhofer and Howard, 1995; Svoboda and Block, 1994; Hunt *et al.*, 1994; Oiwa and Takahashi, 1988; Hill, 1938), the speed will then be approximately proportional to the opposing load, leading to the prediction that reducing the PEF should lead to increased speed of poleward movements. That this is not observed suggests a motor mechanism at the kinetochore that maintains constant speed over a wide range of loads (Joglekar and Hunt, 2002).

This concept of "load independence" was first proposed by Nicklas (1965) based on the observation in grasshopper spermatocytes that the speed of chromosome movements is independent of chromosome size. Skibbens *et al.* (1995) extended this view to include vertebrate mitotic cells and both poleward and antipoleward movement, by showing that the speed of chromosome fragments containing kinetochores is unchanged by laser ablation that leaves them attached to the bulk of the chromosome by only thin, compliant strands of chromatin. Our data provide additional support for load independence, and this conceptually leads to a straightforward explanation for the abrupt changes in direction observed during directional instability. Given that we know both kinetochore forces and PEFs act on the chromosome, and that PEFs do not affect the speed of chromosome movement, it follows that load independence is a property of the kinetochore. Indeed in our experiments, chromosome arm fragment without kinetochores do not maintain a constant speed and may stop oscillating (e.g., Figure 3). If rather than exhibiting a monotonic force-velocity relation, kinetochore motors are load-independent up to the point where they fail, then a chromosome would be expected to move at a constant speed even with an increasing PEF, before abruptly switching directions when the opposing PEF is sufficient to cause failure of the motors at the leading kinetochore. At this point, the motors at the trailing kinetochore, relieved of any opposing forces, can engage unopposed, and will move the chromosome at the same speed in the opposite direction (e.g., Joglekar and Hunt, 2002). It is possible to predict directional instability-like oscillations without invoking load-independence for the underlying force generators, but the speed of movements exhibits greater variability (Civelekoglu-Scholey *et al*., 2006). To maintain constant speeds with such a mechanism requires a delicate balance

of parameters, including the number of force generators, PEF distribution, elastic properties, and the effects of force on microtubule polymerization, such that load on motors at the leading kinetochore is constant during a run toward the pole, but rapidly increases leading up to reversal. In this way, motors at the leading kinetochore would fail before slowing of the chromosome becomes pronounced due to the increasing opposing PEF.

Load independence broadly implies that either 1) the force-generating step in the chemomechanical cycle is not rate limiting, or 2) the chemomechanical cycle can vary in a manner that allows accommodation for changing loads. The first mechanism is established if a process that is independent of the force-generating step in the chemomechanical cycle limits the speed. Since the leading kinetochore follows the tips of depolymerizing microtubules, load independence then implies that the rate of microtubule depolymerization at a kinetochore is not directly affected by the tension on a kinetochore; for vertebrates this significantly constrains the possible mechanisms by which kinetochores maintain attachments with kinetochore microtubules (for review see Maiato *et al*., 2004; Franck *et al*., 2007). As discussed in Joglekar and Hunt (2002), the second mechanism is predicted if microtubules are drawn into kinetochores via interactions with an array of microtubule binding sites as originally hypothesized by Hill (1985). Though Hill proposed that these binding sites are arranged in "sleeves", this geometry is not specifically required, and the binding sites could consist of conventional motor proteins such as CENP-E, which would then generate force in a non-conventional manner (for further discussion, see Joglekar and Hunt, 2002; Thrower *et al*., 1996; Lombillo *et al*., 1995).

The models of Civelekogulu-Scholey *et al*. (2006) and Joglekar *et al*. (2002) both suppose that chromosome reversals are induced by PEFs. As pointed out by Khodjakov *et al*. (1999), this is not a *prima facie* requirement for directional instability, which could arise even if reversals are random and independent of PEFs. By observing changes in the amplitude of directional instability induced by severing chromosome arms, we now establish that PEFs do indeed induce chromosome reversals. Regardless of the specific force generating mechanism at the kinetochores, for PEFs to induce reversals beyond some threshold they must induce all force-generating motors at a leading kinetochore to abruptly fail or disengage. Then, at the maxima of a chromosome's oscillations, the PEF presumably approaches the maximum force that the leading kinetochore can bear before failing. Because the speed of the chromosome remains constant, the more rapidly PEFs approach this threshold as a chromosome moves toward a pole, the smaller the excursion toward the pole, and the amplitude of oscillations. Conversely, if the PEFs increase more slowly, the amplitude of directional instability is increased. Thus, the view that PEFs serve to guide directional instability leads to the prediction that shortening a chromosome's arm should increase the amplitude of direction instability, due to the decreased area on which the PEFs can act. Consistent with this, our result indicated that the oscillation amplitude increases as the length of the chromosome arm shortens (Figure 6B).

As expected, chromosome arms that are severed from the kinetochore region usually cease directional instability. However, some arms, in Figure 3 for example, continue to move in sync with the chromosome for a few cycles after severing, thus appearing to undergo directional instability. These arms eventually move out of the

chromosome cluster, and become out of the sync with the parent chromosome (arm trace after 1000 sec, Figure 3). We hypothesize that synchronization with the chromosome for a few cycles following severing occurs because of steric constraints; much like a person being jostled in a crowd, a chromosome arm is swept along with nearby chromosomes when chromosomes are packed tightly together.

From the relationship between the severed length of the chromosomes and the change in oscillation amplitude, we calculate the PEF distribution to increase sub-linearly with the displacement from the spindle equator (exponent 0.4, Figure 6B). Thus rather than the PEF increasing more steeply away from the equator, as might be expected from a simple view of microtubules as an array of straight rods projecting from a sharp focus, the PEF increases most rapidly near the equator and flattens toward the poles (Figure 6C). To interpret this surprising result, we examined the distribution of interpolar microtubules, which has been determined in PtK cells by reconstruction of serial section electron micrographs (Mastronarde *et al*., 1993). We first calculate the distributions of interpolar microtubule density from left and the right poles for metaphase and early anaphase (Figure 6D). We then estimate the PEF distribution by calculating the "polarity adjusted" density describing the amount that the number of microtubules from one pole exceeds the other, thus accounting for the summation of opposing PEFs developed on opposite-polarity microtubules from opposite poles. The resulting PEF distribution (Figure 6D squares) is consistent with the PEF distribution we estimated from the amplitude of directional instability: the PEF increases most rapidly near the equator, and flattens as the poles are approached (Figure 6C black curve). The PEFs then decrease as the pole is approached, but this falls outside the range of the chromosome oscillations we

observed, taking into account the difference in spindle lengths between species. As estimated by either approach, PEFs are distributed very differently than previously envisioned (Joglekar *et al.*, 2002; Civelekoglu-Scholey *et al.*, 2006). The similarity between the distribution of interpolar microtubules density and the PEF distribution calculated from chromosome oscillations supports the hypothesis that PEFs are proportional to the microtubule density and the size of chromosome arms (Rieder and Salmon, 1994).

Having established that PEFs are responsible for chromosome reversals, we can estimate the force (F) required to cause chromosomes to reverse directions by calculating the PEF generated by the interpolar microtubules at the point where chromosome reverse direction. Assuming the PEF is proportional to interpolar microtubule density and the surface area of the chromosome, $F = kDA$, where k is the PEF per microtubule, D is the polarity adjusted density of the interpolar microtubules in a spindle cross section at the chromosome's location, and A is the cross sectional area of the chromosome facing the poles; the product of D and A estimates the polarity adjusted number of microtubules in contact with the chromosome. Given that data on interpolar microtubule density is not available for newt lung cells but is available for Ptk1, we estimate F for Ptk1 cells. Using data from Khodjakov and Rieder (1996) we observe the locations at which a bioriented chromosome, shown in their figure 1F, reverses direction. Then from the polarity adjusted microtubule density (Figure 6D metaphase), and the *in vitro* PEF per microtubule of 0.5 pN/MT for microtubules in lateral contact with a chromosome (Brouhard and Hunt, 2005), we find the average PEF opposing poleward movements is 4.9 ± 1.1 (avg. ± s.e.) pN at the point the chromosome reverses directions (see

Supplemental Information). This is of similar magnitude to the 25-50 pN estimated by Nicklas for insect meiosis (Nicklas 1988). The force estimate negligibly increases by 0.2 pN if we include a force of 1.1 pN per microtubule polymerizing into a chromosome (Marshall *et al.*, 2001) since the distribution of microtubules shows that very few tips impinge on any given chromosome.

Since viscous drag on a chromosome is negligible (Nicklas, 1965) the sum of the forces from the two kinetochores must balance the PEF. Then, making the potentially dubious assumption that drag from the trailing kinetochore is minimal, we can estimate the maximum force per microtubule at the leading kinetochore by dividing the PEF just prior to switching direction by the number of kinetochore microtubules. Examination of the number of kinetochore microtubules per chromosome in metaphase from Mastronade *et al.*, 1993 Figure 2B revealed three populations of kinetochore microtubules, ones in bundles of 5 (2 bundles), 3 (2 bundles), and 2 (6 bundles). Since at the trailing kinetochore, most of the time there are no depolymerizing microtubules (Joglekar *et al.*, 2002) and kinetochore spends about half time as trailing and half time as leading, we assume the bundles with 2 or 3 microtubules are trailing and both microtubules are polymerizing. We know that poleward force depends on the number of kinetochore microtubules (Hays and Salmon, 1990) and tension increases the number of kinetochore microtubules (King and Nicklas, 2000), and depolymerizing kinetochore are the dominate force generator at the kinetochores (Khodjakov and Rieder, 1996). Therefore, we believe the bundles with 5 microtubules are of the leading kinetochores. Averaging the number of microtubules in the trailing kinetochore, we found that on the average any kinetochore would have 2 polymerizing microtubules. So the number of depolymerizing

microtubules at the leading kinetochores are 3. However, it is likely that the number of depolymerizing microtubules at the leading kinetochore increases as the chromosome approaches the turning point (predicted by Joglekar *et al.*, 2002), it is possible that the polymerizing microtubules at the leading kinetochore becomes depolymerizing as the chromosome approaches the turning point. Therefore, the likely number of depolymerizing microtubules at the leading kinetochore just prior to direction switch is around 3 to 5 for Ptk1 cells. (The total number of microtubules can increase beyond 5 for example. However, there is a limit (King and Nicklas, 2000). The absolute maximum depends on the number of kinetochores per microtubules, around 35 (Joglekar *et al.*, 2002).) Each polymerizing microtubule generates less than 2 pN (Hunt and McIntosh, 1998) and there are average of 2 polymerizing microtubules at the trailing kinetochore. So the total force opposing the leading kinetochore force is approximately 9 pN (5 from net polar ejection force, and 4 from trailing kinetochore). With this information, we estimate the force generated by individual depolymerizing microtubule at kinetochore to be about 2 to 3 pN, in agreement with Hunt and McIntosh, 1998 (<15 pN).

We have applied high-precision ultrafast laser microsurgery to study mitotic mechanics. By severing chromosome arms, we abruptly perturbed the balance of mitotic forces, allowing us to characterize the role of PEFs in direction instability, and explore the mechanisms by which forces are developed to move mitotic chromosomes. The reduction of PEFs has no effect on the speed of movements, but increases the amplitude of directional instability. This establishes that PEFs influence the force generating state at the kinetochores, and constrains the potential mechanisms by which kinetochores generate forces and maintain attachments to spindle microtubules. Our data supports

mechanisms that predict the speed of kinetochore motors is load-independent up to the point they fail, and suggests that the maintenance of microtubule attachments to kinetochores does not involve changing the rate of microtubule depolymerization in response to tension, though this does not exclude an influence on the rate the microtubule switch to growth. From the reduction in chromosome arm length and the associated increase in oscillation amplitude, we calculated the distribution of PEF. Contrary to existing models supposing an increasingly steep concave-up force curve with increasing distance from the spindle equator, the curvature is sub-linear concave-down so that the rate of increase diminishes, possibly approaching a plateau or even dropping near the poles. By describing how force balances influence chromosome movements these studies reveal fundamental mechanics of chromosome segregation, and lay groundwork for advancing mechanistic models of this intrinsically mechanical process.

4.4. Materials and Methods

Laser Micro-Surgical System

These experiments are part of a collective effort to study the mechanics of chromosome congression and segregation that is manifested as directional instability. To do so, we custom designed a laser microsurgery system. This system (Figure 2) has the unique ability of performing fluorescence, phase contrast, and differential interference contrast microscopy while performing surgical operation. For all experiments, we use a Zeiss 100x/1.30 NA Neofluar Phase 3 objective and matching condenser. High-precision ultrafast laser surgery is performed using a diode-pumped Nd:glass chirped pulse

amplification (CPA) laser system (Intralase Corp., Irvine, CA) that generates 600 to 800 fs pulses at a repetition rate of up to 3 kHz. Dichroic and polarized mirrors couple the laser pulses into the illumination light path of an inverted microscope (Zeiss Axiovert 200, Thornwood, NY). These mirrors are selected to avoid interference with normal microscopy, and through careful alignment achieve minimal laser energy loss.

To achieve high precision, the laser is focused to a diffraction-limited spot by completely filling the back focal aperture of the objective. A tri-axial, computer-controlled, piezoelectric stage (Mad City Labs, Inc., Madison, WI) is mounted on top of the regular manual stage to achieve nanometer precision while allowing scanning across a 35mm Petri dish with 14mm microwell (MatTek Corp., Ashland, NY). The optical mounts and the microscope are mounted rigidly to an optical table to reduce vibration and ensure stability. Custom software and design electronics allows control of laser pulse delivery, specimen targeting, and image capture. Taken together, the precision and automation of this unique instrument allow robust cell tracking and laser surgery for investigating mitotic movements in an efficient manner.

Tissue Culture

Primary newt lung epithelial cells are used because they lay flat during mitosis and allow good visualization of chromosomes and the mitotic spindle. Newt lung cultures are prepared as previously described (Poirier, 2001). Briefly, red-spotted newts (*Notophthalmus viridescens*) obtained from Connecticut Valley Biological Supply Co. (Southampton, MA), are euthanized by immersion for 30 minutes in 1 mg/ml tricaine (Sigma #A5040, St. Louis, MO). Using sterile technique, the lungs are dissected, cut into

1 mm^3 pieces, and soaked in L-15 medium supplemented with FBS and antibiotics for 24 hours. The explants are then lightly squashed onto the Petri dish glass, covered with a piece of dialysis filter, and held down by a Teflon ring. Within 7 days, epithelial cells begin to migrate onto the glass, incubated at room temperature (22-25°C). When a few rows of epithelial cells surround the lung fragment, the dialysis filter is removed. Experiments are performed when mitotic activity peaks, about 2 weeks after dissection. Cells are selected for experimentation based on flatness during mitosis, the visibility of centrosomes, and the ability to resolve individual chromosomes.

Laser Ablation

Selected mitotic chromosomes are tracked for a few oscillation cycles, during which images are captured at 1 frame every 2 or 3 seconds. Using laser pulse energy of 2 to 3 nJ/pulse, the laser is scanned in a raster pattern to slice across a chromosome arm. Scans are repeated, once from top of the chromosome to bottom (estimated by the diameter of the chromosome), then again from bottom to top at 10nm steps, to ensure complete ablation. The total volume of the cell ablated is approximately 3 μm^3. The pulse energies of 2 to 3 nJ were experimentally determined to ablate cellular material without causing detectable bubble formation (e.g. Joglekar *et al*., 2003; Ke *et al*., 2005). After ablation, image capture resumes at 1 frame every 2 or 3 seconds.

Chromosome tracking

We developed semi-automatic tracking software that performed cross-correlations on a selected region of interest. This algorithm and operating procedure is similar to that

described in Skibbens *et al.*, but uses National Instrument pattern matching. Additional processing was used to further enhance tracking accuracy, including contrast equalization, image thresholding, and calculating the centroid of the cross-correlations. Reproducibility and accuracy were demonstrated by the tracking stationary objects, and by comparing tracking data for moving objects obtained from multiple operators. Precision is better than a pixel (63 nm at our imaging magnification). Tracking performed by different operators showed some differences in absolute positions due to choice of the region of interest, but superposition of traces from different operators showed identical trends. The accuracy depends on the variability of the chromosome image during the course of an experiment. Rolls, yaws, and pitches decrease the accuracy, especially if a chromosome moves out of the imaging plane. If significant changes in the region of interest occurred, tracking was terminated, or if the chromosome was still clearly identifiable, a new region of interest was selected.

Analysis

During mitosis the entire spindle often moves, and to accurately measure directional instability this must be taken into account. Directional instability was described by Skibbens *et al*. (1993) in terms of the chromosome position relative to one of the centrosomes, and likewise we plot chromosome position relative to one or the other centrosomes. This positional information is then fitted with multiple lines (e.g. lines overlaying data points in Figure 5AB); each line fits the chromosome motion in a single direction within an oscillation cycle. The extent of a chromosome excursion during an oscillation is determined by iteratively changing the intersection of the line fits

73

before and after a direction reversal, until both fits yield the minimum mean square error. The lines are categorized as either poleward movement or anti-poleward movement if the direction of movement persists for more than 10 seconds and if the speed of movement is greater than 1/3 of the average speed of the particular chromosome. This lower bound is imposed to exclude periods where directed chromosome movement, and thus directional instability, are unclear. The speed is calculated from the slope of the line fits. Student's t-test is used to compare the speed of chromosome movement toward and away from the spindle equator, and before and after the laser ablation to show laser ablation did not change the chromosome speed. The oscillation amplitude is calculated as the distance between direction reversals. For each chromosome, the amplitude before and after surgery is compared using Student's t-test.

4.5. Supplemental Information

To calculate the polar ejection force (PEF) opposing the poleward movements, we rescaled the size of the PtK cell spindle (~16 μm) shown in Khodjakov and Rieder (1996) Figure 1A-D to match that shown in Mastronarde *et al*. (1993; ~11 μm), where metaphase microtubule density is available. This allows us to estimate the density, *D*, of microtubules in lateral or end-on contact with a chromosome. The cross-sectional area facing the poles, *A*, was estimated from the product of the length and width of the chromosome, measured from the micrographs shown in Khodjakov and Rieder (1996) Figure 1A-D. The chromosome is most clear in Figure 1D in Khodjakov and Rieder, and we measure it to be about 5.5 μm. The density of microtubule passing through the area

of the chromosome facing a pole was taken as an estimate of the number of microtubules

in lateral contact with the chromosome (primarily generated by the chromokinesin Kid;

Brouhard and Hunt, 2005). For PEF from polymerizing microtubules impinging end-on

against the chromosome, the effective target area is the cross-sectional area facing a pole.

This contributes a relatively small fraction of the total PEF, since the distribution of

microtubule ends predicts that the fraction of polar microtubules that abut end-on against

a chromosome is very small.   Using the values of 0.5 pN per microtubule for lateral

contact (Brouhard and Hunt, 2005) and 1.1 pN for end-on (Marshall *et al*., 2001), we

estimated the force, F, required to cause chromosomes to reverse directions to be 5.1 ±

1.1 pN (avg. ± s.e.) on the average with a range from 0.4 pN to 14 pN depending heavily

on the position of the trip point relative to the spindle equator.

References

Ault, J.G., A.J.Demarco, E.D.Salmon, and C.L.Rieder. 1991. Studies on the Ejection Properties of Asters - Astral Microtubule Turnover Influences the Oscillatory Behavior and Positioning of Mono-Oriented Chromosomes. *Journal of Cell Science* 99:701-710.

Brouhard, G.J. and A.J.Hunt. 2005. Microtubule movements on the arms of mitotic chromosomes: Polar ejection forces quantified in vitro. *Proceedings of the National Academy of Sciences of the United States of America* 102:13903-13908.

Cassimeris, L., C.L.Rieder, and E.D.Salmon. 1994. Microtubule Assembly and Kinetochore Directional Instability in Vertebrate Monopolar Spindles - Implications for the Mechanism of Chromosome Congression. *Journal of Cell Science* 107:285-297.

Civelekoglu-Scholey, G., D.J.Sharp, A.Mogilner, and J.M.Scholey. 2006. Model of chromosome motility in Drosophila embryos: Adaptation of a general mechanism for rapid mitosis. *Biophysical Journal* 90:3966-3982.

Franck, A.D., A.F.Powers, D.R.Gestaut, T.Gonen, T.N.Davis, and C.L.Asbury. 2007. Tension applied through the Dam1 complex promotes microtubule elongation providing a direct mechanism for length control in mitosis. *Nature Cell Biology* 9:832-U171.

Gerlich, D., J.Beaudouin, B.Kalbfuss, N.Daigle, R.Eils, and J.Ellenberg. 2003. Global chromosome positions are transmitted through mitosis in mammalian cells. *Cell* 112:751-764.

Habermann, F.A., M.Cremer, J.Walter, G.Kreth, J.von Hase, K.Bauer, J.Wienberg, C.Cremer, T.Cremer, and I.Solovei. 2001. Arrangements of macro- and microchromosomes in chicken cells. *Chromosome Research* 9:569-584.

Hays, T.S. and E.D.Salmon. 1990. Poleward Force at the Kinetochore in Metaphase Depends on the Number of Kinetochore Microtubules. *Journal of Cell Biology* 110:391-404.

Hill, A.V. 1938. The heat of shortening and the dynamic constants of muscle. *Proceedings of the Royal Society of London Series B-Biological Sciences* 126:136-195.

Hill, T.L. 1985. Theoretical Problems Related to the Attachment of Microtubules to Kinetochores. *Proceedings of the National Academy of Sciences of the United States of America* 82:4404-4408.

Hunt, A.J., F.Gittes, and J.Howard. 1994. The Force Exerted by A Single Kinesin Molecule Against A Viscous Load. *Biophysical Journal* 67:766-781.

Hunt, A.J. and J.R.Mcintosh. 1998. The dynamic behavior of individual microtubules associated with chromosomes in vitro. *Molecular Biology of the Cell* 9:2857-2871.

Joglekar, A.P. and A.J.Hunt. 2002. A simple, mechanistic model for directional instability during mitotic chromosome movements. *Biophysical Journal* 83:42-58.

Joglekar, A.P., H.Liu, G.J.Spooner, E.Meyhofer, G.Mourou, and A.J.Hunt. 2003. A study of the deterministic character of optical damage by femtosecond laser pulses and applications to nanomachining. *Applied Physics B-Lasers and Optics* 77:25-30.

Joglekar, A.P., H.H.Liu, E.Meyhofer, G.Mourou, and A.J.Hunt. 2004. Optics at critical intensity: Applications to nanomorphing. *Proceedings of the National Academy of Sciences of the United States of America* 101:5856-5861.

Juhasz, T., H.Frieder, R.M.Kurtz, C.Horvath, J.F.Bille, and G.Mourou. 1999. Corneal refractive surgery with femtosecond lasers. *Ieee Journal of Selected Topics in Quantum Electronics* 5:902-910.

Kapoor, T.M. and D.A.Compton. 2002. Searching for the middle ground: mechanisms of chromosome alignment during mitosis. *Journal of Cell Biology* 157:551-556.

Kapoor, T.M., M.A.Lampson, P.Hergert, L.Cameron, D.Cimini, E.D.Salmon, B.F.Mcewen, and A.Khodjakov. 2006. Chromosomes can congress to the metaphase plate before biorientation. *Science* 311:388-391.

Ke, K., E.F.Hasselbrink, and A.J.Hunt. 2005. Rapidly prototyped three-dimensional nanofluidic channel networks in glass substrates. *Analytical Chemistry* 77:5083-5088.

Khodjakov, A. and C.L.Rieder. 1996. Kinetochores moving away from their associated pole do not exert a significant pushing force on the chromosome. *Journal of Cell Biology* 135:315-327.

Khodjakov, A., R.W.Cole, B.F.Mcewen, K.F.Buttle, and C.L.Rieder. 1997. Chromosome fragments possessing only one kinetochore can congress to the spindle equator. *Journal of Cell Biology* 136:229-240.

Khodjakov, A., I.S.Gabashvili, and C.L.Rieder. 1999. "Dumb" versus "smart" kinetochore models for chromosome congression during mitosis in vertebrate somatic cells. *Cell Motility and the Cytoskeleton* 43:179-185.

King, J.M. and R.B.Nicklas. 2000. Tension on chromosomes increases the number of kinetochore microtubules but only within limits. *Journal of Cell Science* 113:3815-3823.

King, S.J. and T.A.Schroer. 2000. Dynactin increases the processivity of the cytoplasmic dynein motor. *Nature Cell Biology* 2:20-24.

Konig, K., I.Riemann, P.Fischer, and K.H.Halbhuber. 1999. Intracellular nanosurgery with near infrared femtosecond laser pulses. *Cellular and Molecular Biology* 45:195-201.

Kural, C., H.Kim, S.Syed, G.Goshima, V.I.Gelfand, and P.R.Selvin. 2005. Kinesin and dynein move a peroxisome in vivo: A tug-of-war or coordinated movement? *Science* 308:1469-1472.

Levesque, A.A. and D.A.Compton. 2001. The chromokinesin Kid is necessary for chromosome arm orientation and oscillation, but not congression, on mitotic spindles. *Journal of Cell Biology* 154:1135-1146.

Loesel, F.H., J.P.Fischer, M.H.Gotz, C.Horvath, T.Juhasz, F.Noack, N.Suhm, and J.F.Bille. 1998. Non-thermal ablation of neural tissue with femtosecond laser pulses. *Applied Physics B-Lasers and Optics* 66:121-128.

Lombillo, V.A., C.Nislow, T.J.Yen, V.I.Gelfand, and J.R.Mcintosh. 1995. Antibodies to the Kinesin Motor Domain and Cenp-e Inhibit Microtubule Depolymerization-Dependent Motion of Chromosomes In-Vitro. *Journal of Cell Biology* 128:107-115.

Maiato, H., J.DeLuca, E.D.Salmon, and W.C.Earnshaw. 2004. The dynamic kinetochore-microtubule interface. *Journal of Cell Science* 117:5461-5477.

Maiato, H., P.J.Hergert, S.Moutinho-Pereira, Y.M.Dong, K.J.Vandenbeldt, C.L.Rieder, and B.F.Mcewen. 2006. The ultrastructure of the kinetochore and kinetochore fiber in Drosophila somatic cells. *Chromosoma* 115:469-480.

Marshall, W.F., J.F.Marko, D.A.Agard, and J.W.Sedat. 2001. Chromosome elasticity and mitotic polar ejection force measured in living Drosophila embryos by four-dimensional microscopy-based motion analysis. *Current Biology* 11:569-578.

Mastronarde, D.N., K.L.Mcdonald, R.Ding, and J.R.Mcintosh. 1993. Interpolar Spindle Microtubules in Ptk Cells. *Journal of Cell Biology* 123:1475-1489.

Mcintosh, J.R., E.L.Grishchuk, and R.R.West. 2002. Chromosome-microtubule interactions during mitosis. *Annual Review of Cell and Developmental Biology* 18:193-219.

Meyhofer, E. and J.Howard. 1995. The Force Generated by A Single Kinesin Molecule Against An Elastic Load. *Proceedings of the National Academy of Sciences of the United States of America* 92:574-578.

Mitchison, T.J. 1989. Polewards Microtubule Flux in the Mitotic Spindle - Evidence from Photoactivation of Fluorescence. *Journal of Cell Biology* 109:637-652.

Mitchison, T.J. and E.D.Salmon. 1992. Poleward Kinetochore Fiber Movement Occurs During Both Metaphase and Anaphase-A in Newt Lung-Cell Mitosis. *Journal of Cell Biology* 119:569-582.

Mosgoller, W., A.R.Leitch, J.K.M.Brown, and J.S.Heslopharrison. 1991. Chromosome Arrangements in Human Fibroblasts at Mitosis. *Human Genetics* 88:27-33.

Nicklas, R.B. 1965. Chromosome Velocity During Mitosis As A Function of Chromosome Size and Position. *Journal of Cell Biology* 25:119-&.

Nicklas, R.B. 1988. The Forces That Move Chromosomes in Mitosis. *Annual Review of Biophysics and Biophysical Chemistry* 17:431-449.

Nishiura, M., T.Kon, K.Shiroguchi, R.Ohkura, T.Shima, Y.Y.Toyoshima, and K.Sutoh. 2004. A single-headed recombinant fragment of Dictyostelium cytoplasmic dynein can drive the robust sliding of microtubules. *Journal of Biological Chemistry* 279:22799-22802.

Oiwa, K. and K.Takahashi. 1988. The Force-Velocity Relationship for Microtubule Sliding in Demembranated Sperm Flagella of the Sea-Urchin. *Cell Structure and Function* 13:193-205.

Poirier, M.G. 2001. MICROMECHANICALHEMICAL STUDIES OF MITOTIC CHROMOSOME ELASTICITY AND STRUCTURE.

Pronko, P.P., S.K.Dutta, J.Squier, J.V.Rudd, D.Du, and G.Mourou. 1995. Machining of Submicron Holes Using A Femtosecond Laser at 800-Nm. *Optics Communications* 114:106-110.

Rieder, C.L., E.A.Davison, L.C.W.Jensen, L.Cassimeris, and E.D.Salmon. 1986. Oscillatory Movements of Monooriented Chromosomes and Their Position Relative to the Spindle Pole Result from the Ejection Properties of the Aster and Half-Spindle. *Journal of Cell Biology* 103:581-591.

Rieder, C.L. 1990. Formation of the Astral Mitotic Spindle - Ultrastructural Basis for the Centrosome Kinetochore Interaction. *Electron Microscopy Reviews* 3:269-300.

Rieder, C.L. and E.D.Salmon. 1994. Motile Kinetochores and Polar Ejection Forces Dictate Chromosome Position on the Vertebrate Mitotic Spindle. *Journal of Cell Biology* 124:223-233.

Sawin, K.E. and T.J.Mitchison. 1991. Poleward Microtubule Flux in Mitotic Spindles Assembled Invitro. *Journal of Cell Biology* 112:941-954.

Schnitzer, M.J., K.Visscher, and S.M.Block. 2000. Force production by single kinesin motors. *Nature Cell Biology* 2:718-723.

Skibbens, R.V., V.P.Skeen, and E.D.Salmon. 1993. Directional Instability of Kinetochore Motility During Chromosome Congression and Segregation in Mitotic Newt Lung-Cells - A Push-Pull Mechanism. *Journal of Cell Biology* 122:859-875.

Skibbens, R.V., C.L.Rieder, and E.D.Salmon. 1995. Kinetochore Motility After Severing Between Sister Centromeres Using Laser Microsurgery - Evidence That Kinetochore Directional Instability and Position Is Regulated by Tension. *Journal of Cell Science* 108:2537-2548.

Svoboda, K. and S.M.Block. 1994. Force and Velocity Measured for Single Kinesin Molecules. *Cell* 77:773-784.

Thrower, D.A., M.A.Jordan, and L.Wilson. 1996. Modulation of CENP-E organization at kinetochores by spindle microtubule attachment. *Cell Motility and the Cytoskeleton* 35:121-133.

Waters, J.C., T.J.Mitchison, C.L.Rieder, and E.D.Salmon. 1996. The kinetochore microtubule minus-end disassembly associated with poleward flux produces a force that can do work. *Molecular Biology of the Cell* 7:1547-1558.

Waters, J.C., R.V.Skibbens, and E.D.Salmon. 1996. Oscillating mitotic newt lung cell kinetochores are, on average, under tension and rarely push. *Journal of Cell Science* 109:2823-2831.

Wood, K.W., R.Sakowicz, L.S.B.Goldstein, and D.W.Cleveland. 1997. CENP-E is a plus end-directed kinetochore motor required for metaphase chromosome alignment. *Cell* 91:357-366.

Zhai, Y., P.J.Kronebusch, and G.G.Borisy. 1995. Kinetochore Microtubule Dynamics and the Metaphase-Anaphase Transition. *Journal of Cell Biology* 131:721-734.

CHAPTER 5

STRUCTURAL KNOCKOUT OF AN ASC SPECK RESCUES CELLS FROM APOPTOSIS; THE SPECK IS A PLATFORM FOR APOPTOSIS

5.1. Introduction

ASC, or **A**poptosis-associated **S**peck-like Protein Containing a **C**aspase Recruitment Domain, also known as **T**arget of **M**ethylation-induced Gene **S**ilencing **1**, TMS1, is associated with the eventual secretion of interleukin IL-1β and the activation of nuclear factor NF-κB. IL-1β plays an important role in the regulation of immune response and host defense. However, adversely regulated, it can contribute to increased tumor invasiveness (Apte *et al*., 2006), inflammatory diseases associated with aging (Chung *et al*., 2006), and autoinflammatory syndromes (Galeazzi *et al*., 2006). NF-κB also plays important roles in immune responses and inflammation. When improperly regulated, NF-κB can work in concert with IL-1β to contribute to inflammatory diseases (Tak and Firestein, 2001). ASC is important to the regulation of IL-1β secretion and NF-κB activation.

ASC is a 22-kDa adapter protein composed of a pyrin (PYD) and a caspase recruitment domain (CARD). As an adapter protein, it is capable of interacting with proteins upstream of IL-1β and NF-κB. For example, NALP1, cyropyrin/NALP3, and Caspase-1 are known to form inflammasomes (Martinon *et al*., 2002; Agostini *et al*.,

2004); Caspase-8, 10, and CARD12/Ipaf are known to form an apoptosome (Masumoto *et al*., 2003). Other known interacting partners are pyrin and RICK (Richards *et al*., 2001; Stehlik *et al*., 2003), whose function is less well understood. Through these interacting partners, ASC affects a wide spectrum of pathways critical to apoptotic and inflammatory events.

Apoptosis is correlated with the formation of an ASC Speck. This correlation has been widely reported and as early as in 1999 by Masumoto *et al*. In their paper, it is shown that the percentage of apoptotic cell increases proportionally with the percentage of cells with speck. In their case, speck formation is induced with drugs such as bleomycin or etoposide. We observed similar correlations in HeLa cells transfected with ASC-GFP fusion protein and formed specks without drug induction (Richards *et al*., 2001).

The activation of apoptotic pathway coincides with the formation of a speck. But is the speck an active promoter of apoptosis, or is the speck a byproduct or ancillary component of the apoptotic pathway? Without a method for specifically interfering with the functioning, if any, of a speck, it is difficult to discriminate causation from correlation. However, applying Structural Knockout technology to disrupt a speck abruptly allows direct testing of the hypothesis that the speck is a platform for the apoptotic machinery. Specifically, if a speck mediates apoptotic machinery, a structural knockout of a speck should prevent or delay cell death.

A Structural Knockout is a novel technique that brings intracellular manipulation to a nanoscopic scale while at the same time reducing collateral damages associated with such manipulation. It relies on an ultrafast laser for the ablation of intracellular material

and sophisticated nano-manipulators for targeting. The ultrafast laser pulses, upon reaching critical breakdown intensity, induce nonlinear optical breakdown inside of the cell. The nonlinearity of the optical breakdown is important in providing a breakdown threshold such that damage is induced only above the threshold. Thus, when the ultrafast laser pulses are tightly focused by a high numerical aperture microscope objective, the damage region can be restricted to below the diffraction limit and into the nano-scale regime (Joglekar *et al*., 2003; Joglekar *et al*., 2004). For example, repeatable cuts of trenches as small as 30 nm in width have been demonstrated in borosilicate (Ke *et al*., 2005a), and repeatable holes around 250 nm have been produced in cell membranes (Joglekar *et al*., 2003). Because of the sharp ablation threshold, the focused ultrafast laser pulses produce no damage out of the plane of the focus where the intensity is below the breakdown threshold. Thus, this technique surpasses micropipettes and microneedles in spatial resolution and ease-of-use when applied to disrupt intracellular components.

Structural knockouts can perform functions that are extremely difficult with biochemical techniques such as genetic knockouts, RNAi, and antibody inhibition. These tools alter the expression of specific proteins in cells by over-expression or by the manipulation of genes (knockout, knockdown) to inhibit or reduce protein expression. However, in cells, many processes take place on discrete structures or protein platforms containing multiple protein species (e.g., mitochondria, the microtubule organizing center, filopodia). Other than the manipulation of one or several of the protein species that make up such a structural platform, it has never been possible to study the function of one such platform *in vivo* in the living cell. Structural Knockout can alter one platform while leaving other platforms of the same constituents intact and it can do so

83

with great flexibility in spatial and temporal domain. We apply structural knockout to determine the significance of the speck aggregation without disrupting the physiological function of the soluble cytosolic ASCs by testing whether the removal of speck rescues cells from apoptosis.
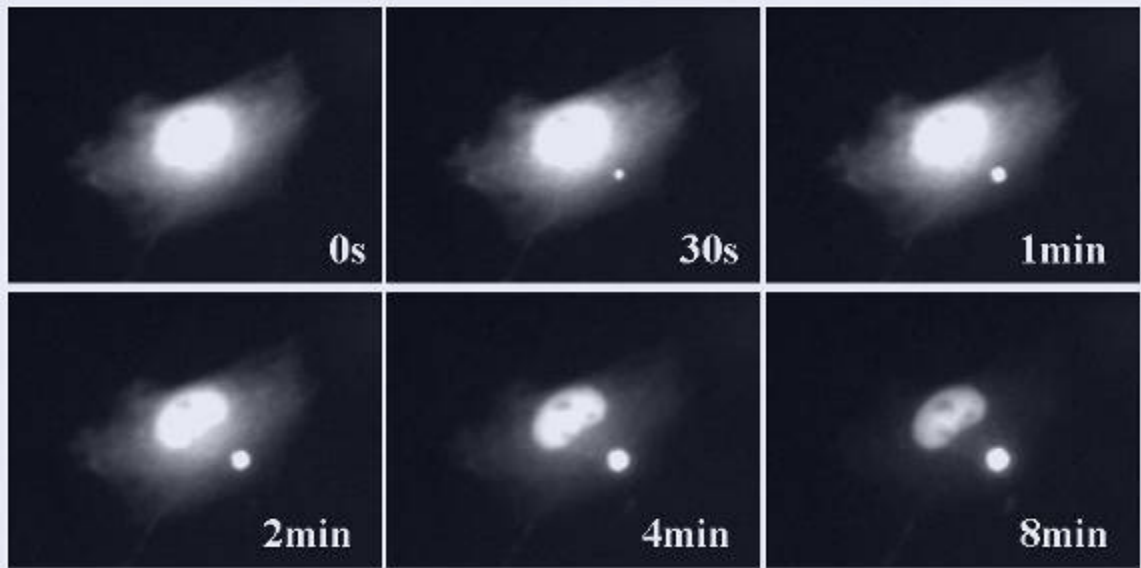
Figure 5.1. Speck formation is fast and depletes cellular ASC. Cellular ASC originally distributed evenly through out the cytoplasm and the nucleus. Upon speck formation, ASC aggregates to a point and, within minutes, cellular ASC is depleted from the cytoplasm. ASC in nucleus takes longer but eventually it will also be depleted.

5.2. Results

Speck Formation is Fast and Depletes Cellular ASC

ASC can form an aggregation called a "speck". The formation of the speck is very rapid, as depicted in Figure 5.1: from not visible to visible, under both phase contrast and fluorescence light microscopy at 20x magnification, takes less than 15 seconds. Speck formation depletes cellular ASC. In HeLa and COS cells transfected with ASC-GFP fusion protein, fluorescently-tagged ASC is distributed throughout the

cytoplasm and the nucleus. Upon speck nucleation in the cytoplasm, ASC aggregates to a point and, within minutes, cellular ASC is depleted from the cytoplasm. ASC in nucleus takes longer but eventually is also be depleted. This depletion of cellular ASC is not due to fluorescence bleaching, as neighboring cells under same excitation light intensity still showed fluorescence of cellular ASC. Although generally free ASCs deplete faster in the cytoplasm (97% out of 32 observations) than the nucleus, in some cases events are reversed (3%). The growth of a speck occurs over a few minutes, after which the speck is micrometers in diameter and takes up a large portion of the cell. Supplemental video S1 shows the formation of an ASC speck. The rapidity in which the speck forms, and the near complete depletion of cellular ASC, motivates our investigation of functional difference between cellular ASC and the aggregated Speck.
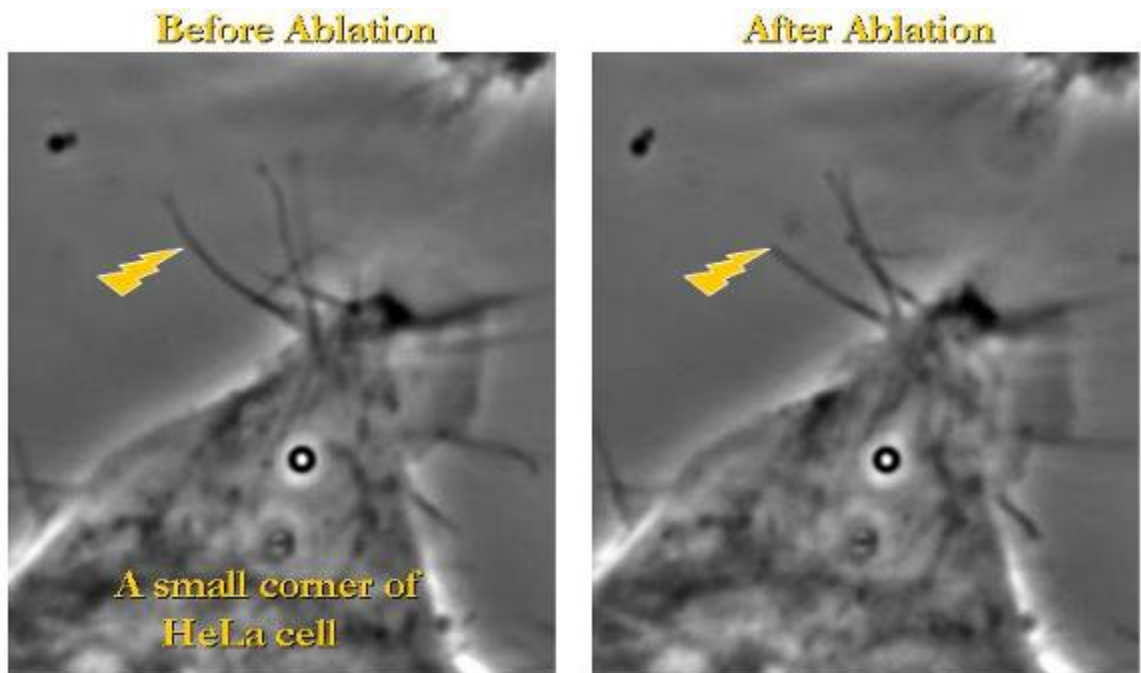

Figure 5.2. Verification of laser targeting and ablation. To verify laser targeting and ablation at 2 to 3 nJ per pulse, the energy used to ablate speck, we ablate extra cellular

protrusions. The protrusions are less than 500nm in diameter thus they act as excellent quality control. Both images are phase contrast of a small corner of HeLa cell under 100x. The image on the left is before ablation and the image on the right is after ablation. The orange inverted lightning indicates where the protrusion is cut.

Specks are selectively destroyed by structural knockout.

To verify laser targeting and ablation at 2 to 3 nJ per pulse, the energy used to ablate speck, we ablate extra cellular protrusions, possibly filopodia, using only a single laser pulse. The protrusions are less than 500nm in diameter thus they provide excellent test target.   This is done before every experiment to make sure that the targeting mechanism and the laser is operating properly.   Figure 5.2 shows an example extracellular protrusion before and after cutting. Both images are phase contrast of a small corner of HeLa cell. The image on the left is before ablation and the image on the right is after ablation. The protrusion has been cut at the location indicated with the small lightning bolt. This pre-experimental test and the following experiment allow us to be certain that the laser is well targeted, and inducing optical breakdown rather than just photo bleaching.
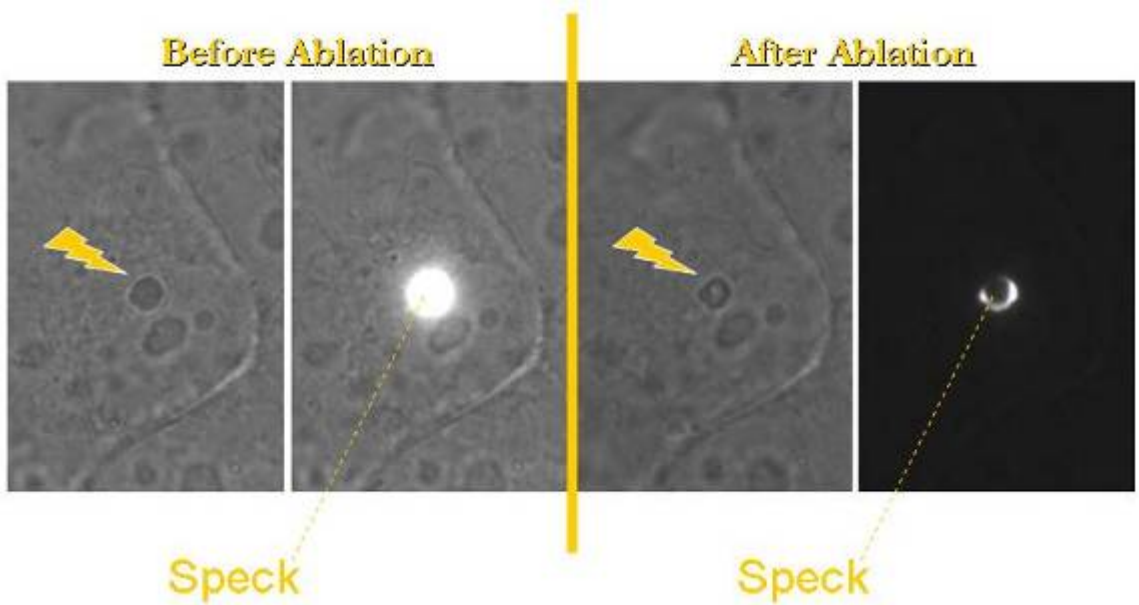
Figure 5.3. The extent of laser damage. To verify the extent of the laser damage, we target the center of a speck. The two images on the left are before ablation, one in phase contrast and the other with fluorescence overlay. The two images on the right are after ablation, one in phase contrast and the other fluorescence. Note that the ring of fluorescence showed the extent of damage within the speck.

To verify that laser damage is restricted to the target area within a cell, we selectively targeted only the center of a speck. Figure 5.3 shows a speck labeled with CFP-ASC in which the center has been ablated, leaving the edges alone. The two images on the left are before ablation, one in phase contrast and the other with fluorescence overlay. The two images on the right are after ablation, one in phase contrast and the other fluorescence. Both fluorescent and phase contrast images reveal that the damage is localized to within the speck.
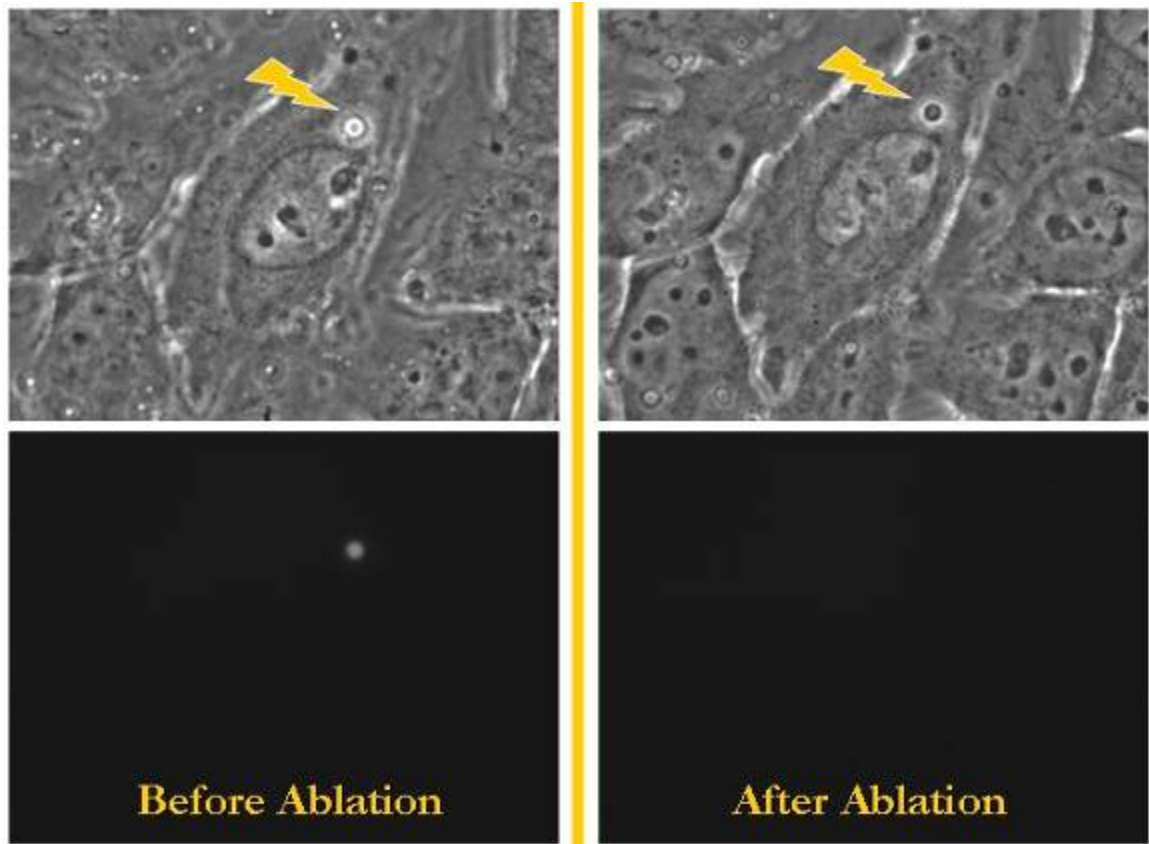
Figure 5.4. An example of speckectomy. The two images on the left are before ablation. The top is phase contrast and bottom fluorescence. The entire speck has been ablated with the laser (indicated by the lightning bolt). The two images on the right are after the ablation. Note that the ablated speck lost its fluorescence.

ASC Speck structural knockout

Figure 5.4 shows an example of a speckectomy. HeLa cells were transfected with YFP-ASC, incubated for 18 hours to allow speck to form, and kept at 36°C to 38°C for the duration of an experiment. Initially a speck is identified by fluorescence, and diameter and height are measured. Then a computer controlled routing moves the stage in a circular pattern, such that the entire speck is removed. Removal of the speck is verified by the absence of fluorescence. Figure 5.4 shows the example cell immediately before and after speckectomy, and Figure 5.5 shows the subsequent cell growth. 2

minutes after ablation, the nuclear membrane is still mostly intact. 4 minutes after ablation, the nuclear membrane begins to disintegrate and chromosomes condense. 27 minutes after ablation, the cell enters metaphase, chromosome lines up in the center of the spindle equator. 1 hour, anaphase. 1 hour and 10 minutes, cytokinesis. 3 hours after the ablation, daughter cells are fully spread. This example is unusual because the cell undergoes mitosis only a few minutes after the ablation; in most observations mitosis in speckectomized cells occurs about 24 hours after the ablation.
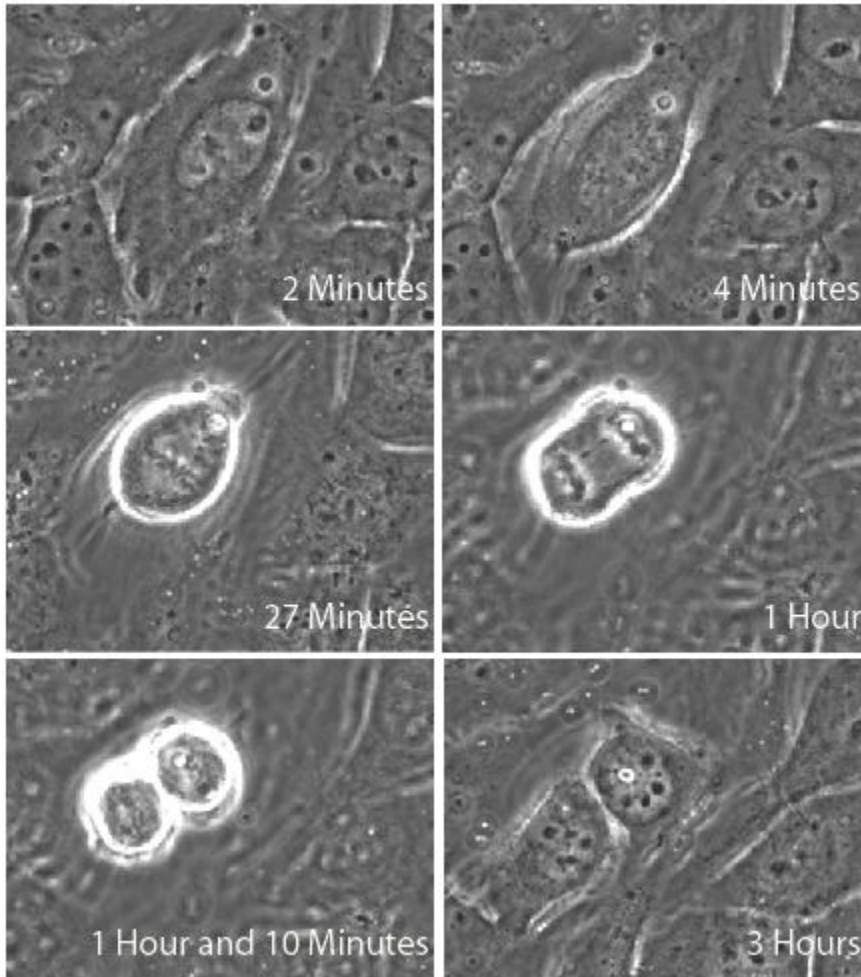
Figure 5.5. Major landmarks of mitosis of a cell that underwent speckectomy. This is the same cell as the one shown in Figure 5.4.

As shown in figure 5.6, of the cells without speck, 100 percent of the cells undergo mitosis (n=34) within 48 hours, while 66 percent of cells with a speck die before dividing and 31 percent undergo mitosis (n=32). In contrast, after speckectomy 100 percent undergo mitosis (n=4). Of these, 3 complete normal mitosis, while one fails to progress beyond metaphase. Thus the fraction of cells that undergo mitosis after speckectomy is the same as that of cells without specks (100%), and is significantly higher than in cells that contain specks ($p < 0.01$).
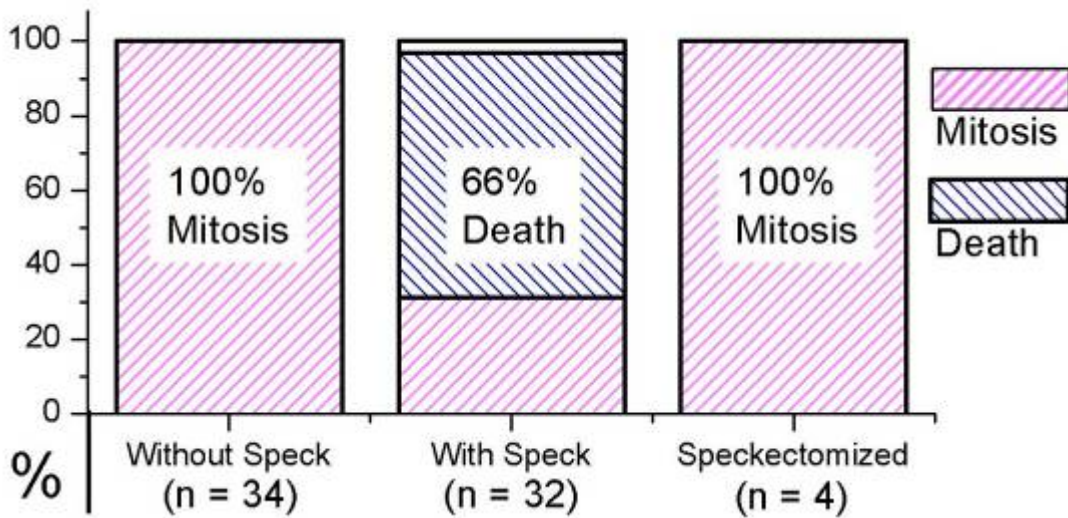
Figure 5.6. Speckectomy rescue cells from apoptosis. HeLa cells are transfected with ASC. Of the cells without speck, 100 percent of cells undergo mitosis. The number of cells tracked is 34. Of the cells with speck, 66 percent died, and only 31 percent undergo mitosis. The number of cells tracked is 32. Of the cells undergo speckectomy, 100 percent undergo mitosis. The number of the cells tracked is four. Of these four, one did not complete mitosis within the 40 hours observation period. The percentage of the speckectomized cells undergo mitosis is same as that of cells without speck and both are 100%. This is significantly higher than the percentage of speck cells undergoing mitosis without speckectomy. The probability of getting four mitoses with speck is less than 1 percent.

Temperature and Speck Induced Apoptosis

It is well established that speck formation is correlated with apoptosis (Masumoto *et al.*, 1999; Richards *et al.*, 2001), and the survival of cells post-speckectomy indicates the relation is causal. However, we find this relation is strongly temperature dependent. Figure 5.7 shows the dependence of cell fate on temperature for ASC transfected cells with and without a speck. For the speck-free cells, the percentages that undergo mitosis are the highest near physiological temperature. As might be expected for mammalian cells, deviations from the physiological temperature, up or down, decrease the percentage of cells that undergo mitosis and increases the percentage that die. In contrast, the cells with a speck showed a drastically different response to temperature change; deviation from physiological temperature increases the percentage of cells that undergo mitosis.
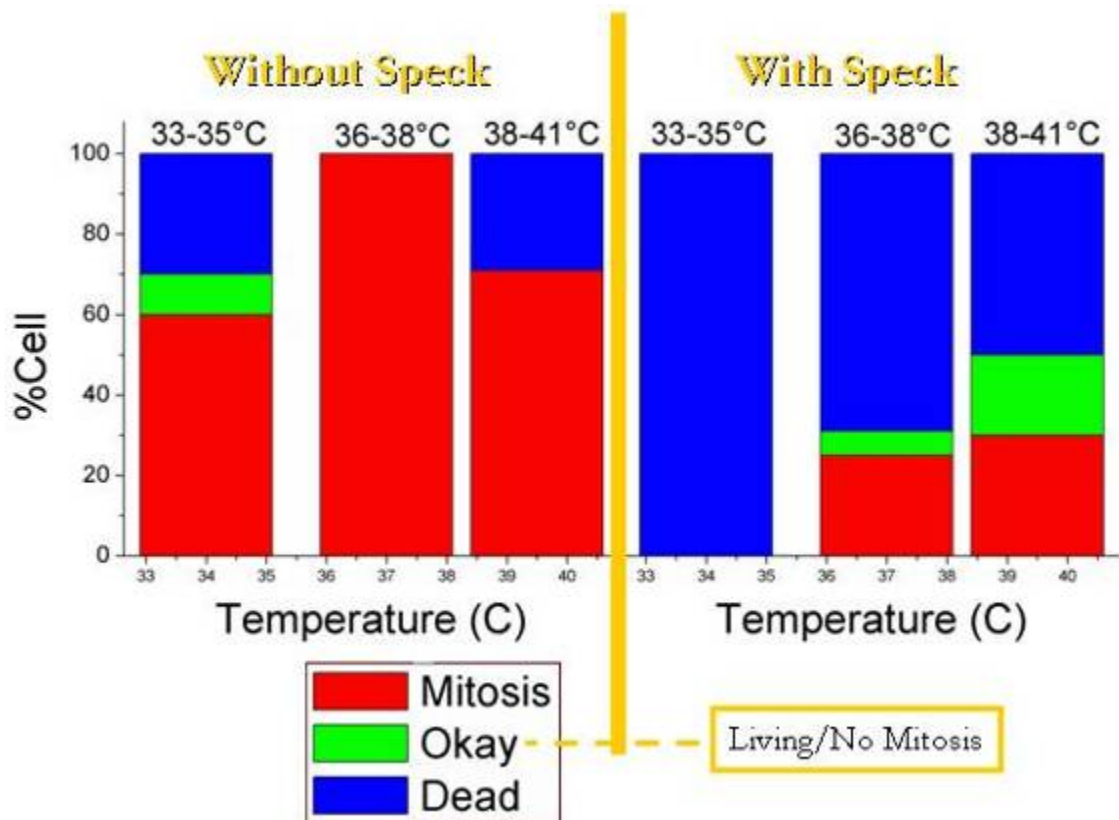
Figure 5.7. The effect of temperature on cell death and mitosis. Deviation from physiological temperature increases mitosis in cells with speck while it decreases mitosis in cells without.

5.3. Discussion

Apoptosis is correlated with the formation of an ASC Speck at physiological temperature. However, higher temperature inhibits the speck mediated apoptotic pathway. Having established this differential relationship between cell fate and temperature for the cells with and cells without speck, we performed our speckectomy experiments near physiological temperature. At this temperature, the percentage of speck cells that undergo mitosis is the lowest, while the percentage of non-speck cells that undergo mitosis is the highest. Our speckectomy results showed that the removal of the

speck prevents cell death and allows cells with speck to undergo mitosis. The near identical percentage of cells without specks and speckectomized cells that undergo mitosis suggests the removal of speck reverts cells to a state prior to the formation of the speck.

The rescue of cells after removal of a speck suggests that the speck is an active platform for apoptotic machinery, which mediates cell death. How can speck act as a platform for apoptosis? We know that in vivo, pro-caspases can be found in high concentration in the speck. Activation of pro-caspases is slow at low pro-caspase concentration. However, at high concentration, pro-caspases rapidly activates itself through a mechanism called proximity induced activation (Salvesen and Dixit, 1999). Thus, it is possible that the speck acts as a platform to agglutinate pro-caspases for proximity-induced activation and, by doing so, activating the apoptotic pathway.

The activation of the apoptotic pathway appears to inhibit the onset of mitosis. In the example described in the introduction, mitosis occurs only a few minutes after the ablation while in all other speckectomy experiments, mitosis occurs around 24 hours after the ablation. The difference between this experiment and the other experiments is that the cells in this experiment is incubated for 64 hours after the transfection instead of the typical 18 hours used for other experiments. It is quite possible that this cell has already has all the mitotic components in place. Progressing to mitosis is stopped by an inhibitory signal from the speck.

The temperature sensitivity of ASC Speck in regulating apoptosis has clinically important implications for understanding autoinflammatory diseases. ASC is known to physically interact with two disease-related proteins: pyrin, the protein that is mutated in

familial Mediterranean fever (FMF) and cryopyrin, the protein mutated in Muckle Wells Syndrome (MWS), Familial Cold Urticaria (FCU), as well as Neonatal Onset Multisystem Inflammatory Disease (NOMID). Patients with FMF suffer from recurrent attacks of fever and localized pain in joints (arthritis), abdomen, chest or skin rash; MWS is characterized by attacks of fever with arthritis and skin rashes; FCU patients display fever, arthritis and skin rash with exposure to cold; and NOMID is a multi-organ inflammatory disease including arthritis, skin rash and meningitis, seen in infants.

All of the diseases mentioned above are sporadic and recurrent, with massive influx of neutrophils into the inflamed sites during attacks. Neutrophils as well as monocytes express cryopyrin, pyrin and ASC. The triggers that precipitate the attacks are unknown, but at least in the case of cryopyrin, one of the triggers is temperature. Interestingly, our results suggest a correlation between temperature and the behavior of cells with ASC specks. We found that high temperature disables speck-mediated apoptosis and allows cells with specks to undergo mitosis. This finding may explain why temperature elevation is needed to increase the viability of macrophages, neutrophils, and monocytes when combating infection. However, it also has pathophysiological implications.

Pyrin, the protein responsible for Familial Mediterranean fever (FMF), co-localizes with ASC speck (Richards *et al.*, 2001). Both ASC and Pyrin are expressed in a tissue-specific manner in neutrophils, monocytes, and macrophages (Richards *et al.*, 2001, Masumoto *et al.*, 1999). These are the cells that through a massive influx invade and cause severe fever and intense pain in areas such as abdomen (peritoneal membranes), chest (pleural membranes), and joints (synovial membranes). It has been

suggested that the modulation of cell survival may play a role in the pathophysiology of FMF (Richards *et al.*, 2001). Indeed, our results show that high temperature prevents apoptosis. It is possible that this is the mechanism that sustains the invasion of immune cells and allows the episodes of FMF to last up to several days.

Using a new advanced laser surgery "structural knockout" which can precisely and selectively ablate intracellular structures, we have demonstrated that the physical aggregate known as a speck actively mediates the apoptotic process, perhaps as a platform to agglutinate and activate apoptotic machinery. Furthermore, we show that temperature influences the speck mediated pathway to modulate cell survival, suggesting this may be a fundamental mechanism linking elevated temperature and inflammatory response, and a mechanism that sustains inflammatory attacks in disease states.

5.4. Materials and Methods

Cell Culture and ASC Transfection.

HeLa cells are grown in Minimum Essential Medium (MEM) containing Earle's Salts (Invitrogen, 11095-098) plus 10% fetal bovine serum. 1.5×10^5 to 2.0×10^5 cells were plated onto 35mm coverslip-bottomed petridish (MatTek, Ashland, MA) 2 days before the experiment. The day before the experiment cell is transfected with ASC-YFP (earlier experiments, ASC-GFP or ASC-FLAG) aided by 1.5 µl of Fugene 6 (Roche, 11814443001) with 1 µg of DNA per petridish. These fusion protein constructs are produced by cloning ASC cDNA into eGFP, eYFP, or eFLAG vectors (CLONTECH). Cells are then incubated for 18 hours at 37C, 5% CO_2. On the day of the experiment, original cell culture medium is replaced with L-15, plus 10% FBS, Pen/Strep, and

95

Fungizone for growth in non- CO_2 rich environment. The Petri dish is sealed with parafilm and transferred by bus, about 1 to 2 miles in 30 minutes, to the lab for experiment.

Speck Formation Video Microscopy.

Speck formation is tracked under 20x phase contrast at 15 seconds per frame. Adobe Photoshop 7.0 is used to batch-convert the image from 16 bits to 8 bits, adjust contrast, and crop the images. Sonic Vegas 4.0 is used to make the speck formation video.

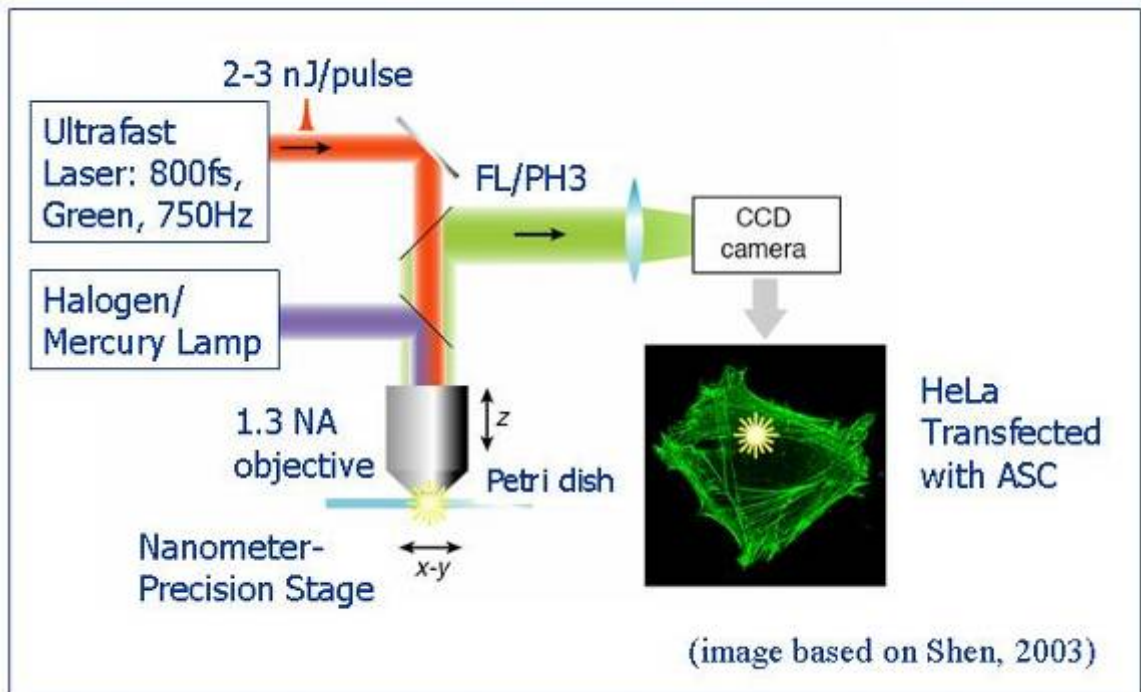**Figure 5.8. Intracellular nanosurgical setup**. An ultrafast laser is used to perform structural knockout. In our case, a green laser 800fs in pulse duration, 750Hz in repetition rate, 2 to 3 nJ in pulse energy is focused by a high numerical aperture microscope objective. These tightly focused ultrafast laser pulses induce nonlinear optical breakdown inside of the cell thus ablating intracellular materials. Nanometer-

precision 3-axes stage allows precise targeting of speck observed under phase contrast and fluorescence microscopy.

Structural Knockout

Critical components required for performing structural knockout are depicted in Figure 5.8. An ultrafast laser, femtoseconds in pulse duration, is used to perform structural knockout. These tightly focused ultrafast laser pulses, upon reaching critical breakdown intensity, induce nonlinear optical breakdowns inside of the cell thus ablating intracellular materials. The nonlinearity of the optical breakdown is important in providing a breakdown threshold such that damage is induced only above the threshold (e.g. see figure 1a in Joglekar *et al*., 2004). Thus, when the ultrafast laser pulses are tightly focused with a microscope objective, the damage region can be sub-light resolution and into the nano-scale regime. The focusing of ultrafast laser pulses also means that the bulk of the laser pulses as it pass through the cell membrane and cytoplasm does no damage because it is below the breakdown threshold. A piezoelectric nanostage (Mad City Labs, Inc., Madison, WI) allows precise targeting of speck observed under phase contrast and fluorescence microscopy.

The small pulse energy and nonlinear relation between energy and optical breakdown by ultrafast lasers prevents collateral damage. Individual pulses during a typical laser micro-surgery are around 2 to 3 nJ (significantly greater than the 0.9 to 1.7 nJ needed for photobleaching with near infrared femtosecond laser pulses passing through 1.4NA objective, Heisterkamp *et al*., 2005). Typical surgery deposits no more than a few micro-joules of energy in total. This is insignificant compared to the energy delivered by halogen or mercury lamps used for conventional microscopy, which deliver

about 6 orders of magnitude higher energies even in one second. Therefore, the energy delivered by heating and conventional linear absorption of light is negligible; damage only occurs in the small volume when the intensity exceeds the abrupt threshold for optical breakdown. Likewise, mechanical damage from bubble formation and associated shock waves are also negligible for the range of pulse energies used in laser micro-surgery (Ke *et al*., 2005b).

The synergistic effect of precision damage and limited collateral damage allows flexible performance of intracellular surgery. This we apply to study the functional role of ASC speck, which is detailed in the next section.

Speckectomy

A laser micro-surgical system was custom designed to perform the structural knockouts, in this case of a speck. A diode-pumped Nd:glass chirped pulse amplification (CPA) laser system (Intralase Corp., Irvine CA) that generates 800 fs pulses at a repetition rate of up to 750 Hz, is brought into the micro-surgical system such that the ability to perform fluorescence, phase contrast, and differential interference contrast microscopy in maintained while performing the surgery. Carefully selected dichroic and polarized mirrors are used to couple the laser pulses into the light path of an inverted microscope (Zeiss Axiovert 200, Thornwood, NY). These mirrors are chosen so that they will not interfere with normal microscopy and through careful alignment achieve minimal laser energy loss.

To achieve optimal spatial resolution, the laser is focused to a diffraction-limited spot by completely filling the back focal aperture of an oil immersion objective (Zeiss

100x Plan Neofluar, 1.3 NA). A tri-axial, computer-controlled, piezoelectric stage (Mad City Labs, Inc., Madison, WI) is mounted on top of the regular manual stage to achieve nanometer precision while allowing an entire Petri dish to be scanned. The optical mounts and the microscope are mounted rigidly to an optical table to reduce vibration and ensure stability. Custom software and design electronics allows complete control and orchestration of laser pulse delivery, specimen targeting, and image capture. Taken together, the highly unique and well coordinated features of this instrument make possible the investigation of ASC speck in an efficient manner.

Before an experiment, testing and calibration are performed to ensure laser and targeting mechanisms are performing as expected. First, we calibrate the stage by etching 5um grids over the range of stage movement. Second, we check the laser beam profile by moving a very thin layer of plastic through the laser beam waist. Then we find the focus of the laser by cutting holes in the glass coverslip. When this is done, extra-cellular protrusions are ablated with a single laser pulse 2 to 3 nJ in pulse energy, the energy per pulse used to ablate the speck, to make sure the laser and the target mechanism work in harmony.

To ablate the speck, fluorescence is used to locate an area with at least 2 cells containing a speck and 2 without. A cell with speck is chosen randomly for speckectomy if the specks are not immediately adjacent the nucleus or plasma membrane, as we have found that shooting holes in the nucleus or plasma membrane can kill the cell within 5 minutes after the ablation. With phase contrast, we measure the speck radius and height. Then moving the laser in circular patterns at 2 to 3 nJ per pulse, 750Hz in repetition rate, remove the entire speck. To ensure the entire speck has been destroyed, removal is

checked by fluorescence. A cell without speck also has the same cytoplasmic volume removed with the laser to be used as control. All in all, each experiment consisted of 3 controls and 1 experimental group. The three controls are No Speck/No Ablation, No Speck/Ablation, Speck/No Ablation, and Speck/Ablation.

Cell fate is tracked for at least 30 hours after the ablation. Cell is exposed to about 200ms of halogen light per minute and 200ms of mercury light every 10 minutes. Both halogen and mercury light is focused by a 0.55 N.A. condenser. The frequency of mitosis and cell death is tallied and Chi Square test is used to determine statistical significance.

5.5. Supporting Information

Video S1. Film of Speck Formation (available on request)

This film shows fluorescence microscopy of speck formation. Speck formation is surprisingly fast. Speck can reach a diameter of one micron within a minute and reach maturation within a few minutes. In the film, the HeLa cell is transfected with a fusion protein of ASC and CFP. Initially, ASC are distributed evenly throughout the cell in the cytoplasm and, as well as, in the nucleus. Upon nucleation, cellular ASC gather and form a speck-like structure. Our structural knockout experiments showed the speck as an apoptotic organelle. The speck continues to grow and reach maturation within 8 minutes. Cellular ASC is virtually depleted from the cytoplasm at this point. Further video showed ASC inside of the nucleus will also eventually be depleted. Analysis of speck formation showed ASC can also be depleted first from the nucleus then the cytoplasm,

but such cases are uncommon. The video is taken at 1 frame per 15 seconds.

References

Agostini,L., F.Martinon, K.Burns, M.F.McDermott, P.N.Hawkins, and J.Tschopp. 2004. NALP3 forms an IL-l beta-Processing inflammasome with increased activity in Muckle-Wells autoinflammatory disorder. *Immunity* 20:319-325.

Apte,R.N., Y.Krelin, X.P.Song, S.Dotan, E.Recih, M.Elkabets, Y.Carmi, T.Dvorkin, R.M.White, L.Gayvoronsky, S.Segal, and E.Voronou. 2006. Effects of micro-environment- and malignant cell-derived interleukin-1 in carcinogenesis, tumour invasiveness and tumour-host interactions. *European Journal of Cancer* 42:751-759.

Chung,H.Y., B.Sung, K.J.Jung, Y.Zou, and B.P.Yu. 2006. The molecular inflammatory process in aging. *Antioxidants & Redox Signaling* 8:572-581.

Galeazzi,M., G.Gasbarrini, A.Ghirardello, S.Grandemange, H.M.Hoffman, R.Manna, M.Podswiadek, L.Punzi, G.D.Sebastiani, I.Touitou, and A.Doria. 2006. Autoinflammatory syndromes. *Clinical and Experimental Rheumatology* 24:S79-S85.

Heisterkamp,A., I.Z.Maxwell, E.Mazur, J.M.Underwood, J.A.Nickerson, S.Kumar, and D.E.Ingber. 2005. Pulse energy dependence of subcellular dissection by femtosecond laser pulses. *Optics Express* 13:3690-3696.

Joglekar,A.P., H.Liu, G.J.Spooner, E.Meyhofer, G.Mourou, and A.J.Hunt. 2003. A study of the deterministic character of optical damage by femtosecond laser pulses and applications to nanomachining. *Applied Physics B-Lasers and Optics* 77:25-30.

Joglekar,A.P., H.H.Liu, E.Meyhofer, G.Mourou, and A.J.Hunt. 2004. Optics at critical intensity: Applications to nanomorphing. *Proceedings of the National Academy of Sciences of the United States of America* 101:5856-5861.

Ke,K., E.F.Hasselbrink, and A.J.Hunt. 2005. Nanofabrication with ultrafast lasers at critical intensity. *Proc. SPIE* 5714:53-62.

Ke,K., E.F.Hasselbrink, and A.J.Hunt. 2005. Rapidly prototyped three-dimensional nanofluidic channel networks in glass substrates. *Analytical Chemistry* 77:5083-5088.

Martinon,F., K.Burns, and J.Tschopp. 2002. The inflammasome: A molecular platform triggering activation of inflammatory caspases and processing of proIL-beta. *Molecular Cell* 10:417-426.

Masumoto,J., S.Taniguchi, K.Ayukawa, H.Sarvotham, T.Kishino, N.Niikawa, E.Hidaka, T.Katsuyama, T.Higuchi, and J.Sagara. 1999. ASC, a novel 22-kDa protein, aggregates during apoptosis of human promyelocytic leukemia HL-60 cells. *Journal of Biological Chemistry* 274:33835-33838.

Masumoto,J., T.A.Dowds, P.Schaner, F.F.Chen, Y.Ogura, M.Li, L.Zhu, T.Katsuyama, J.Sagara, S.Taniguchi, D.L.Gumucio, G.Nunez, and N.Inohara. 2003. ASC is an activating adaptor for NF-kappa B and caspase-8-dependent apoptosis. *Biochemical and Biophysical Research Communications* 303:69-73.

Richards,N., P.Schaner, A.Diaz, J.Stuckey, E.Shelden, A.Wadhwa, and D.L.Gumucio. 2001. Interaction between pyrin and the apoptotic speck protein (ASC) modulates ASC-induced apoptosis. *Journal of Biological Chemistry* 276:39320-39329.

Salvesen,G.S. and V.M.Dixit. 1999. Caspase activation: The induced-proximity model. *Proceedings of the National Academy of Sciences of the United States of America* 96:10964-10967.

Stehlik,C., S.H.Lee, A.Dorfleutner, A.Stassinopoulos, J.Sagara, and J.C.Reed. 2003. Apoptosis-associated speck-like protein containing a caspase recruitment domain is a regulator of procaspase-1 activation. *Journal of Immunology* 171:6154-6163.

Tak,P.P. and G.S.Firestein. 2001. NF-kappa B: a key role in inflammatory diseases. *Journal of Clinical Investigation* 107:7-11.

CHAPTER 6

CONCLUSION AND OUTLOOK

6.1. The Technology

Ultrafast femtosecond laser complements the existing repertoire of tools used in research. When tightly focused and when pulse energy is near the breakdown threshold (OCI), it can be used as a scalpel to surgically remove a region smaller than the light resolution limit with very minimal collateral damage. Table 6.1 compares this technology with other modes of laser machining.

Table 6.1. Comparison of LIOB among different laser machining technologies.

	CW Laser	ns Laser	ps/fs Laser	Tightly focused fs using OCI
Ablated size below light resolution limit				X
Low shot-to-shot variation			X*	X
Nonlinear optical breakdown		X	X	X
Cavitation bubble		X		
Highly damped and long-lived Microbubbles.				X
Damaging shockwave		X		

* True only if the pulse duration is a few picoseconds.

6.2. Application: Nanofluidics

As demonstrated in Chapter 3, tightly focused ultrafast femtosecond lasers can be used to create complicated three-dimensional structures in glass. This ability to rapidly translate idea and design into prototype in a single step can decrease research and development time and save money. Table 6.2 compares photolithographic technique to laser machining using tightly focused femtosecond laser for the fabrication of nanofluidic devices in glass. Taking the advantage of rapid increase in electric field strength when electrodes are spaced near each other, micro-structures fabricated with laser machining can be used to perform fast protein separation. Sanghyun Lee, a graduate student in the lab, is currently pursing laser fabricated Nano Capillary Electrophoresis devices (NCE) as a replacement for bulky chemical analytical systems. The future direction involves ELISA based assay systems.

Table 6.2. Comparison of 3D nanofluidics device fabrication in glass.

	Photolithographic technique	Tightly focused fs using OCI
Easy 3D structure		X
Rapid prototyping		X
Multiple steps	X	
Requires clean room	X	
May require HF etching	X	
Forming whole channel in only glass may require sintering	X	
High-aspect ratio sub-micrometer channels		X
Parallel and batch processing	X	

6.3. Application: Nanopore

In the course of investigating debris extrusion, I found microbubbles formed with tightly focused ultrafast femtosecond laser are surprisingly different from cavitation bubbles formed by lasers with longer pulse duration. These slowly expanding bubbles are highly damped and surprisingly long-lived. Instead of creating damage at the fluid and solid interface, they gently push debris out of long channels. A related phenomena dealing with acoustic node formation that interferes with bubble formation and fluid flow in long channels was published by Lee *et al*., in 2007. With increased understanding of water-assisted femtosecond laser machining, I took on projects that required both the raw power of a bulldozer and the delicacy of a needle. One of these projects is nanopore fabrication, a conical structure hundreds of microns in length (raw power) but with a tip opening as little as 50nm in diameter (delicacy). In collaboration with Jeff Uram and Michael Mayer, we used it to detect in real-time the assembly and the size distribution of nanoparticles (Uram *et al*., 2006a; Uram *et al*., 2006b). The future direction is to functionalize the nanopore with proteins or small molecules to study protein-protein or protein-small molecule interactions. A slightly different direction is to cover the nanopore with a planar lipid bilayer that contains embedded ion channels. The small aperture of the nanopore stabilizes the lipid bilayer and allows the detection of neurotoxins under adverse conditions.

6.4. Applications: Chromosome Ablation and Speckectomy

Having identified the major sources of collateral damage (bubble and shockwave formation) and figured out a bypass, I used ultrafast femtosecond laser as a nanosurgical

tool to study mitosis and apoptosis as shown in Chapter 4 and 5. Many cellular processes involve the formation and rearrangement of multi-protein sub-cellular structures. The ability of tightly focused ultrafast femtosecond laser to precisely remove a targeted structure buried inside of the cell is superior to microneedle in terms of collateral damage and operation, and complementary to gene knockout in terms of capability. Comparison of these three techniques is summarized in Table 6.3. In Chapter 4 (Mitosis), I altered polar ejection force (PEF), one of the forces responsible for chromosome movement during mitosis, and determined its role in mitosis. I found that PEF bias chromosome toward the spindle equator. It also limits amplitude of chromosomal directional instability. In addition, I estimated the distribution of PEFs and found that they do not follow previously postulated distribution. In the future, I will be investigating kinetochore forces, the other major force responsible for chromosome movement during mitosis. In Chapter 5 (Apoptosis), I investigated the purpose of speck formation, an aggregate of ASC and other proteins of apoptotic machinery. Currently, in collaboration with Jun Cheng, Andrea L. Waite, Neil Richards, and, Deborah L. Gumucio, we are investigating the process of speck formation. In the future, we will test how various drugs interferes with speck formation.

Table 6.3. Comparison of different knockout technologies.

	Microneedles	Gene knockout	Tightly focused fs using OCI
Spatial and temporal flexibility			X
Capable of removing multi-protein structures	X		X
Easy to implement		X	X

Low collateral damage		X	X
Will not damage cell membrane		X	X
High spatial precision		X	X
Location specific targeting of subcellular structures	X		X

6.5. Conclusion

With a creative mind, by combining different technologies and different tools with tightly focused ultrafast femtosecond laser, we can create instruments that have higher performance and are cheaper (e.g. NCE), are more sensitive than before (e.g. nanopore), and study phenomena that have proven difficult for conventional techniques (e.g. chromosome ablation and speckectomy). I believe tightly focused ultrafast femtosecond laser is now mature and robust enough for the mainstream.

References

Lee,S., J.L.Bull, and A.J.Hunt. 2007. Acoustic limitations on the efficiency of machining by femtosecond laser-induced optical breakdown. *Applied Physics Letters* 91.

Uram,J.D., K.Ke, A.J.Hunt, and M.Mayer. 2006. Submicrometer pore-based characterization and quantification of antibody-virus interactions. *Small* 2:967-972.

Uram,J.D., K.Ke, A.J.Hunt, and M.Mayer. 2006. Label-free affinity assays by rapid detection of immune complexes in submicrometer pores. *Angewandte Chemie-International Edition* 45:2281-2285.